Chapter 3

The CARPT Facility

3.1 History of Radioactive Particle Tracking

Radioactive particle tracking was first used by Kondukov et al. (1964) who used six scintillation detectors to track a radioactive tracer particle in fluidized beds. The lack of a proper data acquisition system prevented them from obtaining quantitative results. Meek (1972) developed a radioactive particle tracking with six detectors to track solids in a turbulent liquid. The detectors were mounted on an axially moving carriage, in order to maintain the particle within the control volume of the detectors. Since the carriage cannot always keep pace with the tracer particle, the particle often went out of the control volume leading to loss of data. In addition, the use of only a few detectors and analog processing resulted in low resolution. Lin et al. (1985) were the first to develop a novel computer aided radioactive particle tracking facility to study solids motion in a fluidized bed. An array of 12 detectors was used. They showed the existence of multiple circulation cells at low gas velocities, and a change in the direction of solids motion with an increase in gas velocity. Moslemian (1987) improved the data acquisition system of Lin et al. (1985) by introducing digital pulse counters, resulting in faster sampling rates. Devanathan (1991) applied radioactive particle tracking, using a neutrally buoyant particle, to study the liquid phase motion in bubble columns. Details of the technique are discussed in the following sections.

3.2 Working Principle

The use of radioactive particle tracking in bubble columns was first applied by Devanathan (1991) who adapted the Computer Automated Radioactive Particle Tracking (CARPT) technique to study the motion of the liquid phase in bubble columns. A single radioactive particle (the isotope employed was radioactive Scandium, Sc^{46}, emitting γ radiation) was used that was neutrally buoyant with respect to the liquid phase phase being tracked. During an experiment, as the particle moves about in the column tracking the liquid phase which is agitated by the passage of gas, the position of the particle is determined by an array of scintillation detectors, that monitor the γ radiation emitted by the particle. The radiation intensity recorded at each detector decreases exponentially with increasing distance between the particle and the detector. In order to estimate the position of the particle from the radiation intensities, calibration is performed prior to a CARPT experiment by placing the particle at various known locations and monitoring the radiation recorded by each detector. Using the information acquired, calibration curves are established that relate the intensity received at a detector to the distance between the particle and the detector. Once the distance of the particle from the set of detectors is evaluated, a weighted regression scheme is used to estimate the position of the particle at a given sampling instant in time. Thereby a set of instantaneous position data is obtained that gives the positions of the particle at successive sampling instants. Time differentiation of the successive particle positions yields the instantaneous Lagrangian velocities of the particle, i.e., velocities as a function of time and position of the particle. From the Lagrangian particle velocities, ensemble averaging is performed to calculate the average velocities and thereafter the various turbulence parameters of the liquid.

The above is a brief introduction to the working principle of the CARPT technique for measurement of the fluid dynamic parameters of the liquid phase. In what follows, different aspects of the technique and the facility at the Chemical Reaction

Engineering Laboratory (CREL) are discussed, highlighting the improvements and additional changes that have been made as part of this work.

3.3 CARPT Setup

A schematic of the bubble column and CARPT setup is shown in Figure 3.1. The hardware (support structures) of the facility was machined to accommodate both CARPT and CT. The difference in the hardware between the two techniques lies in the configuration of the detectors. In the CARPT technique the detectors are strategically positioned around the column, spanning its entire length (Figure 3.1). Each detector unit is a cylinder 2.125" in diameter and 10.25" long, and contains an active cylindrical NaI scintillation crystal (2" by 2"). The total number of detectors used is varied depending on the size of the column. Typically 16 (14 cm column) to 26 detectors (44 cm column) were used. The detectors are held by aluminium support structures which are in turn supported on four vertical Unistrut bars positioned at 90° intervals around the column. The aluminium support structures were machined such that they project at 22.5^0 angles from the Unistrut bars. Therefore, the detectors can be held at eight different angular positions with respect to the axis of the column. Each detector is held on the aluminium support structure such that the axis of the detector is perpendicular to that of the column and the circular face of the detector is tangential to the wall of the column at a given location. The positions of the detectors are measured in cylindrical coordinates. For each detector, with its circular face tangential to the wall of the column, it is thus assumed that the axis of the detector is along the radial coordinate of the column. Hence, accurate alignment of the detectors to conform with cylindrical geometry is necessary, since any misalignment leads to error in location of the particle position. Steel wire braces allow the position of the detectors on the aluminium supports to be adjusted both in terms of radial and angular positions. These support structures can also be moved axially on the Unistrut beams thereby allowing different axial positions for the detectors.

The general configuration of the detectors is shown in Figure 3.2. Two detectors are positioned at a given axial level, at 180 degree angle to each other, i.e., the two detectors are made to face each other, placed on either side of the column. These two detectors form a pair. At the next higher level, the angular position of the next pair of detectors is increased by 45 degrees, from that at the level below. Such a configuration ensures equal spacing between all the detectors in all directions. This is the optimum configuration since it enables the particle to always be close to a set of detectors anywhere in the column, except close to the distributor, below which no detectors are placed.
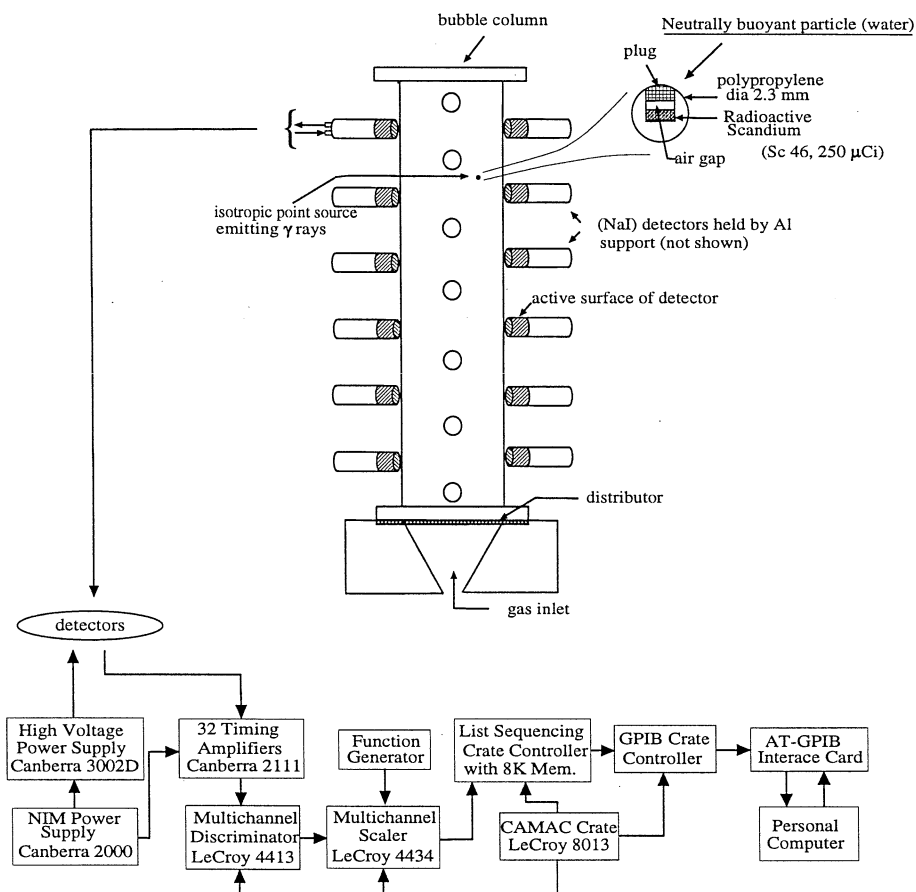

Figure 3.1: Schematic of the CARPT Facility

Bubble columns of three internal diameters, 14 cm, 19 cm and 44 cm were used in this investigation. All the columns are made of Plexiglas. The plenums used for distribution of the gas and liquid into the column are constructed with

Plexiglas as well. All experiments were conducted at atmospheric conditions using compressed air and tap water. Specific details of the experimental conditions along with the distributors used are given in Chapter 4 in which the experimental results are discussed.
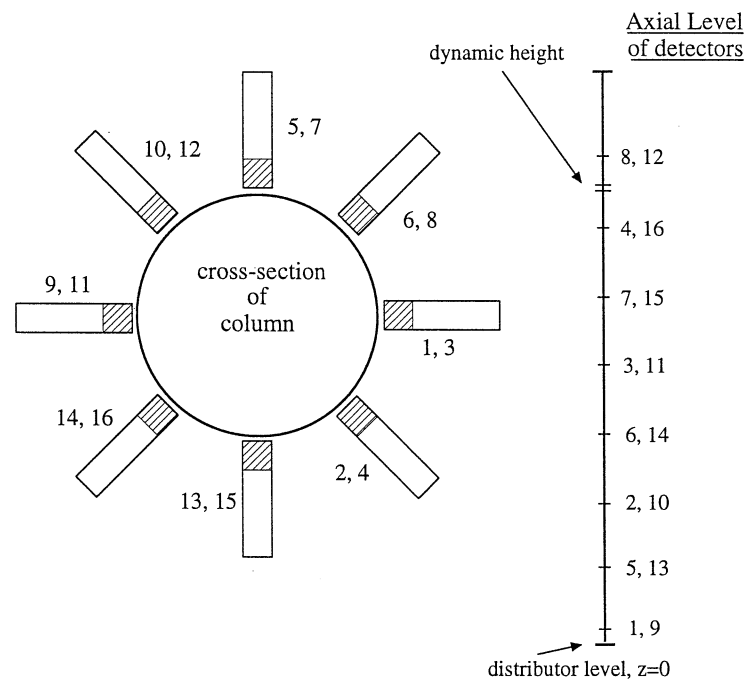

Figure 3.2: Configuration of Detectors in CARPT Experiments

3.4 Radioactive Particle

Scandium-46 was used as the radioactive source in all the CARPT experiments. Sc-46 has a half life of 83.5 days and exhibits two photopeaks at 0.889 MeV and 1.13 MeV. Since Scandium is of high density (2.99 g/cm^3), in order to make a tracer particle that is neutrally buoyant, the small scandium particle is embedded in a polypropylene sphere of outer diameter 2.36 mm, along with a pocket of air, that results in a composite (polypropylene, scandium and air) sphere that has a density very close (e.g. 0.9995 to 1.0005 g/cm^3) to that of water, i.e. 1. The method of tracer preparation is similar to that employed by Devanathan (1991). However, in the present method, instead of using a solid cylinder (0.7 mm by 1.0 mm) of scandium as

done by Devanathan (1991), several smaller particles (about 10 of 100 μ m size) were embedded in the polypropylene sphere, in order to provide more freedom for adjusting the weight and thereby the density of the tracer particle, which was done by trial and error. Hereafter, 'particle' refers to the composite tracer particle (polypropylene, scandium and air).

Care was taken to initially make the particle of slightly 'lighter' density (0.95 g/cm^3) than that of water. Subsequently the particle was sent to the Reactor Research Facility in the University of Missouri at Columbia, for irradiation to approximately 250 μ Ci (for the larger column of 44 cm diameter a target strength of 400 μ Ci was used). Once irradiated, and prior to the experiments the particle was coated with refractory paint which served several purposes. The first was to adjust the density of the particle in order to match, as close as possible the density of the particle with that of water ($\rho_p \sim 0.9995$ g/cm^3). Polypropylene is mildly hydrophilic and slowly imbibes water, as a result of which the particle becomes heavier with increased exposure to water, i.e., over 5 to 6 hours. Coating the polypropylene with paint, therefore, provided a protection for the particle against water, and thus helped in maintaining the density of the particle over the entire duration of the experiment. Finally, the coating of paint also served to reduce the solid liquid interfacial tension and improve the wetting characteristics of the particle, thus lowering the possibility of bubbles sticking to the surface of the particle during an experiment. Such an event reduces the effective density of the particle, which is undesirable.

For all the experiments performed as part of this investigation, the density of the particle was adjusted in order to yield a rise velocity of 0.1 to 0.25 cm/sec. Visual observation of the response of the particle to mild agitation in liquid indicated that the particle was able to follow the liquid well.

3.4.1 Ability of Tracer Particle to Follow the Liquid

In the present CARPT experiments, the measurement of the liquid phase fluid dynamics in a bubble column using a neutrally buoyant finite size spherical tracer particle

(2.36 mm) as a liquid tracer, is based on the assumption that the particle ideally follows the fluid element. The extent to which the particle actually follows the liquid phase plays an important role in the accuracy of the measurement of the liquid velocities using this technique. Close matching of the density of the particle (0.9995 g/cm^3) with that of water ensures that the particle is neutrally buoyant (rise velocities of 0.1 to 0.25 cm/s) However the finite size of the particle makes it differ from a liquid element, unable to sample the small scale eddies. Particle Reynolds number, defined as $Re_p = d_p v_{ps}/\nu_l$, ranges from 2 to 6, where d_p is the particle diameter and v_{ps} is the settling/rise velocity of the particle in water.

The theory of particle motion in a turbulent flow field is complex. The behavior of particles of various sizes and densities is of interest in sediment transport, atmospheric dispersion and flow visualization. A brief background on the equation governing the motion of spherical particles in a viscous turbulent fluid, and some approaches used for solution of the governing equation, which are relevant to the existing situation, are discussed.

The motion of a spherical particle in a turbulent fluid was first described by Tchen (1947) as an extension of the Basset-Boussinesq-Oseen (BBO) equation:

$$\underbrace{\frac{\pi d_p^3}{6}\rho_p \frac{dv_p}{dt}}_{1} = \underbrace{3\pi\nu_l\rho_f d(v_f - v_p)}_{2} + \underbrace{\frac{\pi d_p^3}{6}\rho_f \frac{dv_f}{dt}}_{3} + \underbrace{\frac{1}{2}\frac{\pi d_p^3}{6}\rho_f \frac{dV_{f-p}}{dt}}_{4} +$$

$$\underbrace{\frac{3}{2}d_p^2\rho_f\sqrt{\pi\nu_l}\int_{t_0}^{t}dt'[\frac{dV_{f-p}}{dt'}/\sqrt{t - t'}]}_{5} \tag{3.1}$$

The equation is a force balance and considers the acceleration of the particle (term 1) to be affected by the drag force in the Stokes regime (term 2), the pressure force on the sphere due to the acceleration of the fluid (term 3), the added mass term (term 4) and the Basset history integral which refers to the particle motion for all times from the initiation of motion of the particle (term 5). This equation has been modified by many (Hjelmfelt and Mockros 1966; Maxey and Riley 1983) and used by various researchers in several investigations, among which those that are of relevance to the

present study are discussed here. Most of the interest in studying particle motion in a turbulent flow field (gas phase) is restricted to very small heavy particles ($\rho_p/\rho_g \sim$ 1000), which is not of interest here.

Devanathan (1991) used the BBO equation considering steady flow and neglecting the Basset term. He showed that for a particle size of 2.36 mm and a difference of 0.01 g/cm^3 in density between the particle and the liquid, the maximum difference in the velocities (particle and liquid) is 1 cm/sec.

In the above analysis only steady flow was considered, and in addition, the Basset term was neglected. It has been shown that for a particle suspended in a fluid with varying frequencies of motion, the Basset History term becomes important (Mei et al. 1991; Maxey and Riley 1983; Hjelmfelt and Mockros 1966), by assisting in maintaining parity between the particle and fluid motion. The Basset history term is hence, considered important for this analysis. The analysis can be extended by considering a spectrum of velocities at different frequencies similar to the works of Hjelmfelt and Mockros (1966), and Kuboi et al. (1974).

Hjelmfelt approached the solution of the original Equation 3.1 (including all the terms) by expressing v_f and v_p in terms of their Fourier integrals, and relating the particle velocity in terms of the fluid velocity by means of an amplitude ratio (AR) and a phase angle (PA). The ratio of the respective energy spectra was also obtained. The expressions were obtained in terms of the density ratio (ρ_p/ρ_f) and Stokes number N_s ($\sqrt{\nu_l/\omega d_p^2}$). This definition of the Stokes number is the inverse of the conventional definition ($\sqrt{\omega d_p^2/\nu_l}$). Hjelmfelt's approach has been experimentally verified by Lee and Durst (1982), who performed experiments with particles in turbulent duct flow. Following the approach of Hjelmfelt (1966) for the existing conditions of the CARPT experiment, with the particle size and density ratio mentioned above (Stokes regime of flow is assumed), calculations show that the AR reaches 1.001 and PA, 0.0005, at $N_s = 0.020$. Using the expression for Stokes number, the maximum frequency at which the particle can be taken to follow the liquid up to 99.0% (amplitude ratio) is 30 Hz.

Meek (1972) performed an experimental and theoretical investigation to study the behavior of particles of various densities and sizes in a turbulent liquid flow field, using the modified BBO equation. He showed that the ratio of the turbulent fluctuating velocities of the particle to the liquid, in isotropic homogeneous flow can be obtained as:

$$\frac{\overline{v_p'^2}}{\overline{v_f'^2}} = \frac{1 + \beta^2 p}{1 + p} \qquad (3.2)$$

where β is defined as

$$\beta = \frac{3\rho_f}{2\rho_p + 1} \qquad (3.3)$$

and parameter p is the ratio of the particle response time to the Lagrangian integral time scale.

$$p = \frac{\tau_p}{\tau_L} = \frac{d_p^2}{3\nu_l \beta} \frac{1}{\tau_L} \qquad (3.4)$$

Although the parameter p, for the case of the CARPT tracer particle, will be relatively large (order of 1), since $\rho_p = 0.9995$, $\beta = 1.0007$, which ensures that the ratio of the fluctuating velocities is very close to unity, $v_p'^2/v_f'^2 = 1.0003$. This gives an estimate of the magnitude of the *rms* velocity of the particle in comparison with that of the fluid. The *rms* velocity represents an integral of the energy spectrum $\int_0^\infty E(\omega)d\omega$, and hence covers the entire frequency range.

A combination of the above analyses shows that for frequencies ≤ 30 Hz, which represent the large scale eddies, the particle will be able to closely follow the liquid phase, and the measured particle fluctuating velocities can be considered to be those of the liquid phase. For the higher frequencies, due to its size, the particle will not follow the liquid very closely. However, such frequencies correspond to small length scales and therefore low energy in the power spectrum (for example, see Hinze (1975) for the energy spectrum related to single phase flow turbulence). Recently, Mudde et al. (1997) reported the energy spectrum for two-phase flows in bubble columns, based on LDA measurements, in the bubbly and transition flow regime. The peak in the energy spectrum was shown to occur at 0.1 to 0.5 Hz, depending on operating conditions.

The cascade of energy in the inertial subrange was shown to follow the -5/3 power law of Kolmogorov, for the cases reported. Calculation of the energy content of the velocities, based on Lagrangian measurements using CARPT, also indicate a peak in the energy in the range of 0.1 to 1 Hz. Although the Lagrangian based spectrum is different from the traditional Eulerian energy spectrum, in the power dependence of energy on frequency, qualitatively, the two spectra show similar trends, in as much that the energy content decreases with increase in frequency (Tennekes and Lumley 1972). Using the results of Mudde et al. (1997) for the energy spectrum obtained by LDA, one can show that the energy content of the velocities with frequencies greater than 30 Hz is less than 2 % of the energy of the velocity fluctuations between 0.1 and 30 Hz. Hence, the velocities with frequencies greater than 30 Hz do not contribute significantly to the overall fluctuating *rms* velocities.

If one considers a small scandium particle, 100 μm in radius, with a density of $\rho_p = 2.99$, then $\beta = 0.429$ and the particle response time is $\tau_p = 0.012$ s. This yields $v_p'^2 / v_f'^2 = 0.955$, which indicates that the particle *rms* velocity is 2.2 % lower than the fluid *rms* velocity.

3.5   Signal Processing and Data Acquisition

The CARPT facility developed by Devanathan at the Florida Atlantic University is of the third generation. Some aspects of the data acquisition in the third generation CARPT have been improved in order to achieve faster data transfer rates and, hence, increase the sampling frequency capacities of the technique. This has lead to the fourth generation CARPT, which was designed and developed at the Chemical Reaction Engineering Laboratory (CREL) by Yang (1992). Details of the data acquisition steps involved are described below.

A schematic of the data acquisition system and signal processing for the existing setup is shown in Figure 3.1, along with a schematic of the bubble column facility during CARPT experiments. The system is equipped to use up to a maximum of

32 scintillation detectors. Each scintillation detector containing 2" by 2" NaI crystal with an integral ten stage photo-multiplier tube (PMT) is used to detect the gamma radiation emitted from the scandium particle. The function of the scintillation detector is to convert the energy from the incident gamma radiation into detectable light. When a gamma photon is incident on the NaI crystal of the detector, it releases light photons which get multiplied on the photocathode of the photo-multiplier tube. Biasing of the cathodes of the detectors (1kV) is provided by two high voltage power supplies (Canberra, Model 3002D). Anode pulses are generated at the output of the PMT. One such anode pulse is produced for every gamma photon impinging the crystal of the detector. The pulses produced at the PMTs are still low and are further amplified by passing through timing filter amplifiers (Canberra 2111). The amplifiers accept both positive and negative pulses from the detectors and deliver output pulses in the range of ± 5V. Each timing filter amplifier has independent adjustments for the differential and integral time constants in their RC-CR circuits. These knobs enable us to shorten the tail of the pulse and choose a suitable amplitude for the pulse, respectively. The integral time constant thereby allows one to adjust the intensity of the signal detected (final reading on the computer), for a given source strength. The power to the amplifiers is fed by the NIM/BIN power supplies (Canberra 2000). The raw signal from the amplifiers contains both the primary emissions of the gamma radiation from the source and undesired secondary emissions that arise due to interaction of the gamma radiation with the medium. Since most of the secondary emissions are characterized by fairly low energy radiation, their contribution is effectively removed by feeding the signals from the amplifiers to discriminators. The threshold on the leading edge discriminators (LeCroy 4413) is set to eliminate signals below that threshold. The threshold for the discriminators is continuously adjustable from 15 mV to 1 V by software control. For the CARPT experiments using Sc[46], a threshold of 15 mV, which is the lowest level, is found to be adequate for removing most of the secondary emissions. For each input signal that exceeds this threshold, the discriminator issues a logic pulse, thereby registering only those signals (photons)

that have a certain maximum energy. The pulses from the discriminator are counted using a multichannel 24 bit scaler, which is a binary counter. The scaler has a temporary buffer for each channel to store the accumulated counts. A list sequencing crate controller with 8K first in - first out (FIFO) memory acts as a buffer when contents of the scaler are emptied at user specified rates. When the FIFO is half full a CAMAC (Computer Automated Measurement and Control) crate controller transfers the contents from the FIFO to the hard disk of the computer via a General Purpose Interface Bus (GPIB IEEE 488). The transfer of the data from the scaler to the FIFO memory, and from the FIFO memory to the computer hard drive proceed in parallel with no data errors or loss. The advantage of the CAMAC is that it allows a wide range of modular instruments to be interfaced to a standardized crate. The data acquisition program for the fourth generation CARPT, written in C language utilizes the fast access memory in the CAMAC crate. It can therefore be used to sample at very high frequency rates of up to 500 Hz. In the present experiments, the sampling frequency is set at 50 Hz.

3.6   Calibration

For a given source strength, the intensity of radiation received at a detector from the radioactive particle, decays exponentially with distance between the detector and the source, due to factors such as attenuation and buildup. This is also a complex function of column geometry and the medium being traversed, and hence the gas holdup. In order to estimate the location of the particle from the radiation intensity counts measured at the detectors, calibration is necessary under the given operating conditions (in-situ calibration).

3.6.1   Calibration Procedure

Calibration experiments for CARPT involve positioning the radioactive tracer particle at several hundreds of known locations throughout the column and measuring the

intensity counts received at the detectors. The calibration device (Figure 3.3) used for performing the calibration essentially consists of a hollow frame that is fixed onto the top flange of the column, such that the center of the frame is aligned with the
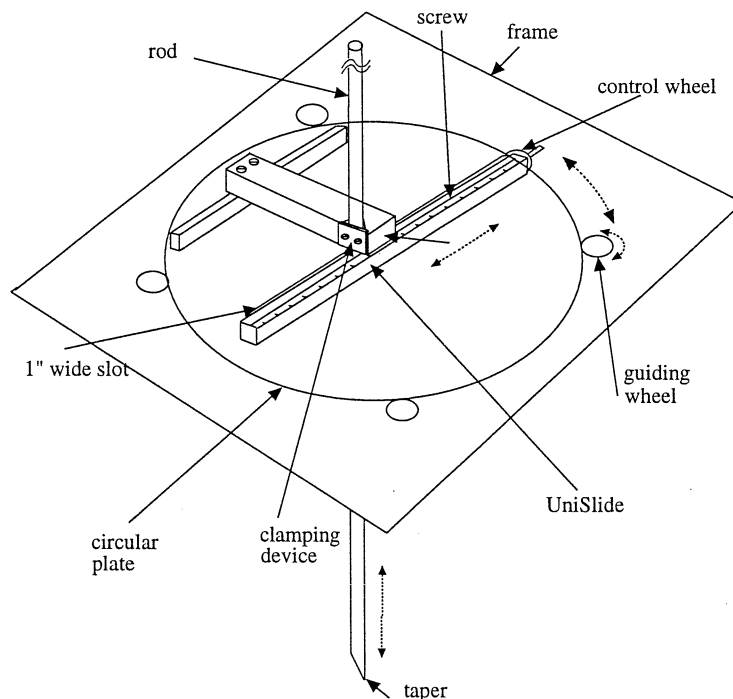
Figure 3.3: Calibration Device

axis of the column. Placed on this frame is a circular plate that is positioned between four guiding wheels which allow for the plate to rotate about the axis of the column. Marks on the frame are made to indicate various angular positions. A one inch wide slot is machined on the plate which passes through the center of the plate, extending from one end of the plate to the other. Fixed on the plate, in alignment with this slot, is a UniSlide control. Mounted on the UniSlide is a clamping device to hold a stainless steel rod 1.25 cm in diameter. The entire rod consists of four sections that can be screwed together with perfect alignment, thus allowing for the use of only certain sections of the rod depending on the (height) requirement at a given time. The bottom tip of the rod is machined with a taper, at the tip of which the tracer

particle is held with a plastic sheet. The clamping device is precisely machined to ensure that the rod is vertical, especially when the particle on the tip of the rod is positioned at the bottom of the column. Vertical movement of the rod allows for the axial positioning of the particle, while the UniSlide control knob determines the radial position of the particle. The rotation of the plate provides for the angular movement. The above device allows for the precise movement of the particle to known locations in the column, using which in-situ calibrations were performed for the various experimental conditions investigated. During a calibration, for a given position of the particle, 256 to 512 samples (intensity counts) are acquired and the data is averaged to obtain mean counts at each of the detectors.

3.6.2   Calibration Curves and Tracer Particle Location - Accounting for Effects of Solid Angle

Once calibration is performed, this yields a set of data for each detector that relates the intensity counts measured to the distance between the particle and the detector. As mentioned earlier, the intensity in a given medium decays exponentially with distance between the particle and the detector. The exact functional form of this relationship is complex and depends on many factors such as attenuation of gamma photons directly reaching the detector by the medium traversed, buildup of the photons caused by the interaction of the primary photons with the medium causing the photons to get deflected from their original path, the solid angle between the particle and the detector, the efficiency of the detector, etc.

The most significant factor is the attenuation of the radiation that results in the exponential decrease of intensity with distance. Consider a single beam of gamma ray traversing a medium of width 'd'. The fraction of the ray that passes through the medium without any interaction is given by Beer's law:

$$I = I_o \exp(-\mu d) \tag{3.5}$$

where μ is the attenuation coefficient of the medium being traversed, I_o is the intensity at the source and I is the intensity measured at distance 'd'. For an isotropic source such as the CARPT tracer particle which emits gamma radiation in all directions, this simple relation becomes more complex, and all the other factors mentioned above become important. However, since attenuation is still the dominant factor affecting the intensity measured, for experimental purposes, the intensity is considered to be a one dimensional function of distance between the particle and detector, and expressed using Taylor's expansion of Beer's law:

$$I = f_p(\frac{1}{d}) \tag{3.6}$$

where f_p is a polynomial function for each detector (Devanathan 1991). Thus, the intensity-distance curves are fitted with polynomial functions of varying degrees, using which a set of distances of the particle from the detectors can be estimated. From these distances the position of the particle is calculated by least squares regression.

Such a relationship, as used by Devanathan (1991), assumes that the intensity is a monotonic function of distance. This is true if attenuation was the only factor affecting the intensity detected, which is the case when using collimated detectors such as in CT (Kumar 1994). However, in CARPT, due to the low strength of the tracer particle, the active surface of the detector comprises both the front circular surface and the side cylindrical surface. In such cases, the intensity cannot be considered as a function of distance only, as illustrated in the graph for a set of calibration data in Figure 3.6, where the same values of the intensity (x-axis) correspond to more than one value of distance. This is primarily due to effects of solid angle, which is discussed in greater detail shortly. The ultimate method of handling the complex behavior of the radiation, is by modeling the various interactions of the gamma radiation to simulate the intensity measured at the detector for a given source strength and medium. This is a complicated task, as it involves in depth modeling of the radiation and its interaction with the medium and detectors, and is beyond the scope of this work. Modeling of the gamma ray interactions using Monte Carlo

simulations has been successfully performed by Larachi et al. (1994) who have used radioactive particle tracking to study the behavior of solids in ebullated beds. Such an effort of modeling the radiation measured at the detector from the source particle by Monte Carlo simulations, is currently underway at CREL by Yang and Gupta (1996).

For the present study an improvement over the original algorithm for estimating particle positions is made by taking into account the effects of solid angle, and thereby modifying a one dimensional relationship of intensity versus distance, to a two dimensional dependence of intensity on the distance and solid angle. The nature of the influence of solid angle and the necessary modifications made to account for these effects is discussed below.

Effects of Solid Angle

The solid angle subtended by the detector at the location of the source is defined as the ratio of the number of photons emitted per second within the space defined by the contours of the source and the detector, to the total number of photons emitted by the source. In other words, it is the fraction of number of photons emitted by a point isotropic source that enter the detector.

$$\omega = \frac{\text{number of photons "seen" by the detector}}{\text{number of photons emitted by the source}} \qquad (3.7)$$

For a point (isotropic) source along the axis of the detector (with a circular face), the solid angle can be calculated using a standard geometrical expression (Tsoulfanidis 1983). From Figure 3.4,

$$\omega = \frac{A_s}{4\pi R_s^2} \qquad (3.8)$$

$$A_s = \int dA = \int_0^{2\pi} \int_0^{\theta_0} R_s^2 \sin\theta \, d\theta \, d\phi = 2\pi R_s^2 (1 - \cos\theta_0) \qquad (3.9)$$
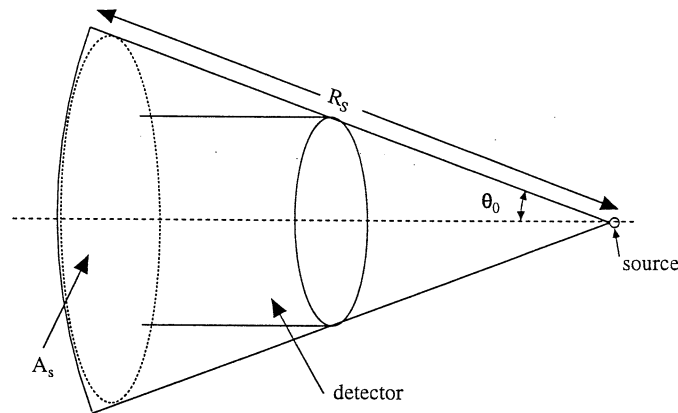
Figure 3.4: Figure for Calculation of the Solid Angle Between an Isotropic Source and a Detector with a Circular Aperture, with the Source on the Axis of the Detector

The effect of the solid angle becomes important when the particle does not lie on the axis of the detector. In such cases computation of the solid angle becomes complex. The source particle now 'sees' both the front face (circular) of the detector as well as the cylindrical side (see insert in Figure 3.5). Consequently, a given distance of the particle from the detector could result in different intensities measured by the detector, depending on the solid angle. In other words, there are multiple values of the distance that result in a particular value of the intensity, depending on the solid angle. This results in the presence of arcs in the distance vs intensity calibration data as shown in Figure 3.6.

Monte Carlo simulations have been performed (Wielopolski 1977; Verghese et al. 1972; Gardner and Verghese 1971) for computation of solid angle subtended at a point source by circular discs and cylindrical surfaces, and algorithms are available for this purpose. In the present work, the algorithms of Gardner and Verghese (1971) and Verghese et al. (1972) have been used to compute the solid angle of the particle placed at various locations with respect to the detector. The graph in Figure 3.5 shows the solid angle as a function of distance for various perpendicular heights (the
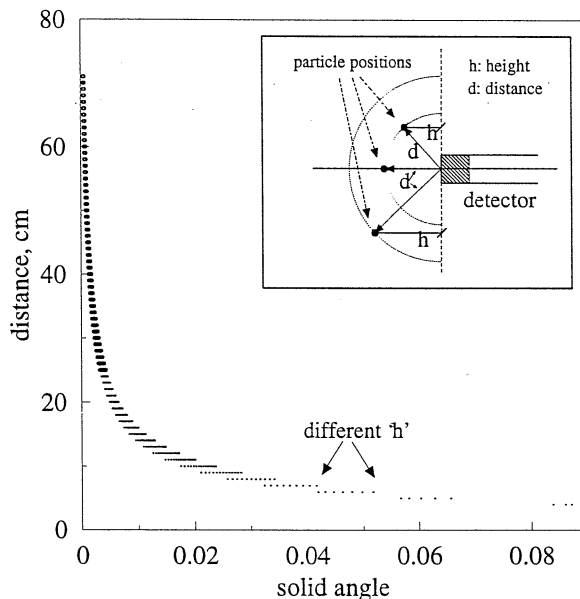
Figure 3.5: Simulations of Distance Vs Solid Angle for Various heights Corresponding to Various Particle Positions

perpendicular distance from the particle to the plane defined by the circular face of the detector). These results can be directly compared with the data from the calibration experiment (typical results shown in Figure 3.6), in which arcs are seen, which suggest that the arcs arise due to the effects of solid angle. These effects of solid angle have to be properly accounted for in estimating the position of the particle, since it is clear that the intensity measured at the detector is not a function of distance alone. The manner in which this is done is described below.

The essence is to modify the algorithm to estimate the distance of the particle from each of the detectors with greater precision. Once the best estimate of the distances is obtained, the position of the particle is calculated by the weighted least squares approach originally formulated by Lin et al. (1985) using linear regression theory (Draper and Smith 1981). In an ideal situation a set of three distances would be sufficient to calculate the x,y,z coordinates of the particle. However, due to the random noise in the radiation data, which arises from the statistical nature of the
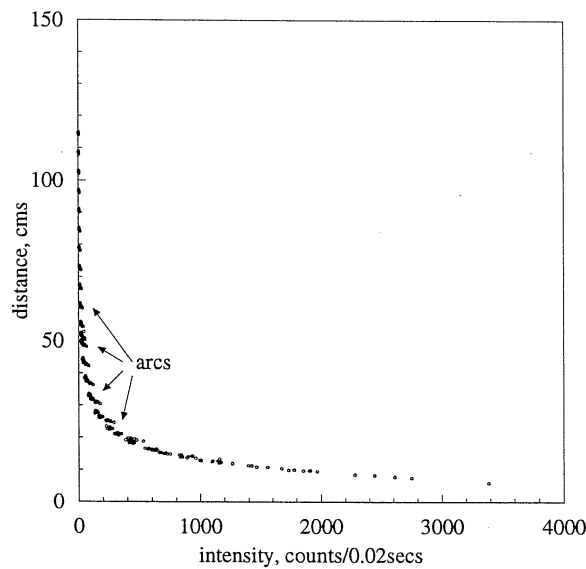
Figure 3.6: Distance Vs Intensity in a 14 cm column (Calibration data for detector 11)

gamma ray emission, a redundancy in the number of detectors is used to minimize the error in estimating the particle position using a weighted least square approach. A weighting matrix is used to weight each detector with a factor that is proportional to the intensity of the radiation measured by that detector, which corresponds to the reliability of the detector measurement. Since this method of weighted least square regression, originally proposed by Lin et al. (1985), is the same as used by Devanathan (1991) and others, the details involving the calculation is omitted here.

The procedure for accounting for the effects of solid angle in estimating the distance of the particle from each of the detectors is discussed below. The tracer particle, during calibration, is placed in an orderly fashion at different locations in the column so as to cover the entire flow field. Typically, a number of (x,y) (or (r,θ)) locations are chosen, for a given axial (z) level, which constitute a horizontal cross-sectional plane. During calibration, the particle is placed at all the selected (x,y) positions for several such axial locations. The resulting intensity counts versus distance data when plotted result in a graph as shown in Figure 3.6. In Figure 3.6 all the points in an 'arc' correspond to particle positions that belong to a particular

cross sectional plane. Qualitatively, Figure 3.6 can be compared with Figure 3.5 which shows the distance versus solid angle. For the particle positions in a cross-sectional plane, although the variation in distance between particle and detector is not much, a relatively significant variation of the solid angle causes an increased variation of the intensity measured (x-axis in Figure 3.6), resulting in the 'arcs'. Therefore, by associating the particle at a given location with an 'arc' in the distance versus intensity curve, it is possible to account for effects of solid angle, in better estimating the distance between the particle and detector. This is done by formulating a two step procedure described below.

1. In the first iteration, the entire set of calibration data is used to obtain the intensity-distance curves by cubic spline fitting. Using these calibration curves for each of the detectors, a first estimate of the particle position is made using the non-linear least square regression method (Devanathan 1991).

2. In the second iteration, only a section of the calibration data is used. This set of data corresponds to the particle positions in a cross-sectional plane at a given axial level which is within ±5 mm of the estimated axial position of the particle. The data constitutes an 'arc' in the intensity vs distance calibration curve and is fitted to a second order polynomial function. If the estimated position of the particle is greater than 5 mm from a calibration plane, interpolation of the data is done to obtain the required set ('arc') of data. The distances evaluated in this step are more accurate than those from the first step, since only the segmented curve corresponding to a particular 'arc' of the data is used. This results in a different functional dependence of the distance on intensity, when compared with step 1. In this manner, the effects arising due to solid angle are accounted for. This refined set of distances is used to re-estimate the position of the particle, which is the final estimated position.

This two step procedure significantly decreases the error in estimation of particle position. For example, the average error in estimating the position of the particle

is reduced from 1 cm to 0.3 cm, in a 19 cm diameter column. To successfully use this method, it is important to get the best possible first estimate of the particle position (and thereby axial position). The best fit of the data to a monotonic function for the dependence of intensity on distance is obtained using cubic splines (NAG software).

3.6.3 Error in Estimating Stationary Particle Positions

Calculation of the error is based on measurements made during the time of calibration, by placing the particle at several known locations in the column, other than the calibration positions, at a given gas velocity. Typically, the particle is placed at 15 to 20 different known locations that span the entire flow domain. In addition to these points, the intensity counts measured during calibration, that serve as calibration data, are also used for recalculating the particle position.

For each position of the particle, the intensity counts that are acquired over 256 to 512 sampling instants at a frequency of 50 Hz, are averaged to yield the mean counts. The set of mean intensity counts for all the detectors is used to estimate the position of the particle using both the two-step iterative algorithm described above and the single step method based on the entire calibration curve. The error in estimation along the x, y and z directions are used to determine the overall location error, calculated as $e = \sqrt{(e_x^2 + e_y^2 + e_z^2)}$.

A comparison of the errors obtained using the two methods of estimation is given in Table 3.1 for randomly selected conditions. As seen in Table 3.1 the error is reduced from an average of 1.4 cm to less than 0.4 cm by the two step procedure. The error close to the distributor is much higher than in the main section of the column. The reason for this is due to the asymmetry in the medium near the distributor, caused by the presence of the flange, especially when the particle is close to the wall. Placing detectors below the distributor is of no avail, and only worsens the situation, due to the exceptionally high attenuation in the medium between the particle and the detector in this region, caused by the presence of the plenum (solid plexigas). This results in significantly low counts measured by the detectors below (or the same level

as) the distributor near the plenum, despite the close proximity of the particle to these detectors, which cannot be captured by the intensity vs distance curves. Hence, the positions close to the distributor ($z \leq 5$ - 8 cm), result in higher errors. For this reason, the column averages reported in Table 3.1 only consider the data away from the distributor. Results indicate that the two-step procedure for estimating the particle position considerably reduces the location error, and such a procedure is necessary for better estimation of the particle positions.

Table 3.1: Comparison of Errors in Estimating Particle Location

Col. Dia.	Sup. Gas Velocity	Average Error	
cm	cm/s	One-step cm	Two-step cm
14	2.4	1.55	0.26
14	12.0	1.31	0.28
19	12.0	1.38	0.31

The column average location error under various operating conditions considered is reported in Table 3.2, along with the average error close to the distributor. There is no effect of gas velocity on the mean location error in a given column size.

Table 3.2: Errors in the Estimation of Stationary Particle Position Using the Two-Step Iterative Algorithm, Under Various Operating Conditions

Col. Dia. cm	Gas Velocity cm/s	Col. Average Error, cm	Std. Dev. cm	Error Near Distr., cm
14	2.4	0.26	0.171	1.2
	4.8	0.22	0.167	1.5
	9.6	0.28	0.235	1.1
	12.0	0.28	0.198	1.5
19	2.0	0.28	0.139	0.7
	5.0	0.27	0.165	1.2
	12.0	0.31	0.281	0.7
44	2.0	0.73	0.681	2.5
	5.0	0.78	0.754	2.7
	10.0	0.76	0.652	2.8

However, the error increases for the largest column diameter of 44 cm. This is due to the increase in the size of the column which causes a greater spread of the calibration data as shown in Figure 3.7. The hollow circles in the figure denote the experimental calibration data points for the 44 cm diameter column. The solid lines are representative data for a 14 cm column, which are drawn to denote the increase in the
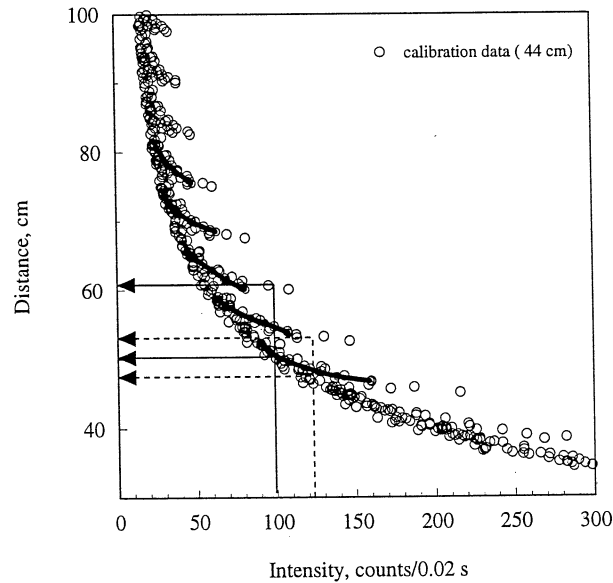

Figure 3.7: Calibration Data of Distance versus Intensity in a 44 cm Diameter Column (solid lines are representative data for a 14 cm diameter column)

spread of the 'arcs' in the 44 cm column. Due to this, the error in estimating the initial estimate of the particle position, using step 1, is higher than that for a small diameter column, thereby resulting in an increase in the final error (using the two step procedure). This increase of error with column size is an inherent characteristic of the present least square regression approach, based on the distance versus intensity functional representation. In order to decrease the error in the data, the radiation at the detectors would have to be modeled using Monte Carlo based simulations to account for the spread in the data. Nevertheless, for the present situation, the relative error of estimation, i.e., $\frac{e}{R}$, from column to column is still the same at ~ 3 %, which is deemed acceptable.

3.7 Computation of Fluid Dynamic Parameters from CARPT Instantaneous Position Data

CARPT experiments are typically conducted for a long time (15 to 40 hrs, depending on size of the column) during which the γ radiation emitted by the radioactive tracer particle, as it follows the liquid, is measured at every sampling instant at a frequency of 50 Hz. The instantaneous positions of the particle at every sampling instant are then estimated from the radiation intensity measurements at all the detectors, using the algorithm described above. Therefore CARPT experiments first result in a set of instantaneous position of the particle over the entire duration of the experiment. Time differencing of these positions yields the instantaneous Lagrangian velocities of the particle, as a function of time and position of the particle. These instantaneous Lagrangian velocities are then used to calculate the time averaged velocities and the various turbulence parameters through out the flow field in the column.

3.7.1 Sampling Compartments

In order to obtain the time averaged fluid dynamic parameters as a function of position in the column, the column is first divided into sampling compartments of certain dimension, depending on the size of the column. There are several ways for discretizing the column as shown in Figure 3.8. Method 'A' which was used by Devanathan (1991) consists of dividing the column, which is essentially a cylinder, in equal divisions along the r, θ and z directions.

Due to the cylindrical coordinate system, this method of discretization results in unequal volumes of the sampling compartments with varying radial location. Hence the compartments in the center of the column, $r \sim 0$, are much smaller than the compartments close to the wall. As a result, for a given duration of a CARPT experiment, the compartments in the center always have very poor statistics relative to the ones close to the wall. In order to improve the statistics at the center, one would have to run the experiment for much longer times.

A. constant Δr, Δθ   B. Constant compartment volume

C. constant Δr, variable Δθ
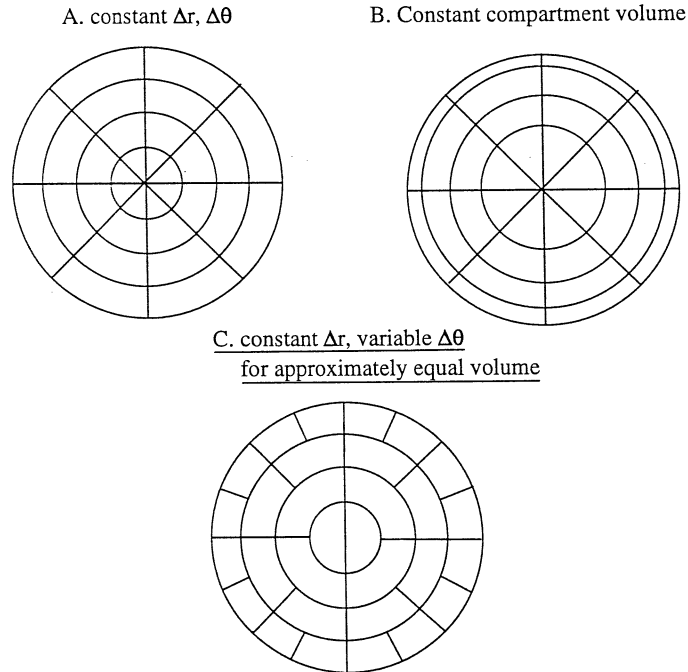for approximately equal volume

Figure 3.8: Column Discretization for CARPT Data Processing

In view of this shortcoming, Devanathan (1991) suggested an alternative method of discretization, method 'B', in which the divisions along the radial direction are varied in order to maintain similar volumes throughout the cross-section. However, such a discretization results in very small Δr close to the wall, almost the size of the tracer particle, ~ 0.2 cm, and therefore reduces the occurrences close to the wall significantly, although the compartment volumes are about the same.

In order to address the above problem, the new discretization method labeled 'C' in Figure 3.8 is used in which the radial and axial divisions are kept constant. $\Delta \theta$ is varied with radial position in the column, so as to maintain reasonable uniformity in cross-sectional area of each compartment, and thereby volume. By using such a discretization, the statistics (number of occurrences of the particle) in each compartment is maintained reasonably uniform. This reduces the time of experiment required to get good statistics throughout the column, in compartments both at the center and at the wall.

The number of divisions assigned to the column varies with size of the column. Table 3.3 shows the assignment of the compartments for the three column sizes used. Δr and Δz are constant as a function of 'r' and 'z', respectively. $\Delta\theta$ varies with radial position. The compartment assignments shown in Table 3.3 were found to be the optimum choice, which was a trade-off between the size of each compartment and the total experimental time.

Table 3.3: Assignment of Compartments to Each Column for CARPT Data Processing

Col. Dia. cm	N_r $\Delta_r = \frac{R}{N_r}$	$N_\theta{}^a$	N_z	Δz^b cm
14	8	2,4,4,8, 8,8,8,16	70	1.7 - 1.9
19	8	2,4,4,8, 8,8,8,16	70	1.7 - 1.9
44	12	2,4,6,8, 10,10,12,14, 16,18,20,24	100	1.7 - 1.9

^{a}entries in this column correspond to each radial compartment starting from 1 to N_r

^{b}varies with dispersion height

Local Mean Velocities

Time differencing of subsequent positions of the particle yield instantaneous Lagrangian velocities. Let x_1, y_1 and z_1 be the coordinates of the particle at a given sampling instant (position 1 and time 1) and x_2, y_2, z_2 be the coordinates at the next sampling instant (position 2 and time 2). The midpoint of (x_1,y_1,z_1) and (x_2,y_2,z_2) is calculated as x, y, z (and a corresponding r, θ, z in cylindrical coordinates). The compartment to which (x, y, z) or (r, θ, z) belongs is calculated, by determining the compartment indices of the midpoint (i, j, k). The velocity calculated by time differencing of (x_1,y_1,z_1) and (x_2,y_2,z_2), as shown in the equations below, is assigned to this compartment with indices i, j and k.

$$u_r(i,j,k) = \frac{r_2 - r_1}{\Delta t} \tag{3.10}$$

$$u_\theta(i,j,k) = \frac{(\theta_1)r}{\Delta t} \tag{3.11}$$

$$u_z(i,j,k) = \frac{z_2 - z_1}{\Delta t} \tag{3.12}$$

In such a manner the instantaneous velocities can be calculated for every sampling instant, as the particle moves around the column following the liquid. Interpretation of the results for the velocity measurements is done by ensemble averaging, which involves averaging the instantaneous velocities measured in a compartment over the entire duration of the experiment. As discussed earlier, in Chapter 2 this ensemble averaging is equivalent to the phasic averaging applicable for modeling.

If N_v is the number of times the midpoint of two successive particle positions falls in a cell with indices (i,j,k), then, the ensemble averaged velocity for the compartment with indices (i,j,k) is

$$\overline{u}_p(i,j,k) = \frac{1}{N_v} \sum_{n=1}^{n=N_v} u_{p,n}(i,j,k) \quad p = r, \theta, z \tag{3.13}$$

Once the ensemble or time averaged velocities are calculated, the various turbulence parameters, such as the turbulent shear stress, normal stresses and kinetic energy can be calculated, from the fluctuating velocities. The fluctuating velocity is defined as

$$u_p'(i,j,k) = u_p(i,j,k) - \overline{u}_p(i,j,k) \tag{3.14}$$

Typically, the turbulent stress is calculated as

$$\overline{u_p' u_q'}(i,j,k) = \frac{1}{N_v} \sum_{n=1}^{n=N_v} u_{p,n}'(i,j,k) u_{q,n}'(i,j,k) \tag{3.15}$$

where again p and q denote the components of the velocity in cylindrical coordinates.

Azimuthal Averaging of Data

If T_{dim} is the number of azimuthal divisions for a given radial locations, the azimuthal averaged velocity is obtained from

$$\tilde{u}_p(i, k) = \frac{\sum_{j=1}^{T_{dim}(i)} \overline{u}_p(i, j, k) N_v(i, j, k)}{\sum_{j=1}^{T_{dim}(i)} N_v(i, j, k)} \qquad (3.16)$$

Results for the various turbulence parameters are similarly averaged.

Typical comparison of results after CARPT data processing, using different types of compartment discretizations, described earlier, are shown in Figure 3.9 for the time averaged axial liquid velocity and the turbulent kinetic energy in a 14 cm column. The different discretizations all result in the same trend for the profiles of the velocity and the turbulent kinetic energy. However, results for the case with finer discretization show more scatter. This arises due to the relatively poor statistics in this case (denoted by the inverted triangle in Figure 3.9), since the volume of each compartment is reduced by 4 when compared with the data for the coarser discretization, represented by the circle in Figure 3.9. All the three cases are considered for the same experimental data, obtained for a total time of 18 hrs. Comparison of methods 'A' and 'C' (refer to Figure 3.8) for the same N_r and N_z in Figure 3.9, shows that the two are very nearly the same, except toward the center of the column for the turbulent kinetic energy. Near the center, when using method 'A', with equal θ divisions for all radial locations, the volume of the compartment is considerably reduced, thereby lowering the statistics in this region. The optimum choice of compartment discretization is the one with the best statistics, denoted by the circle in Figure 3.9, which is also reported in Table 3.3.

CARPT Computation of the Lagrangian Correlation Coefficients

The above parameters are all based on an Eulerian framework (velocities are denoted by u), i.e., the parameters are related to measurements at fixed position or compartment. With the CARPT technique, essentially the Lagrangian velocity of the
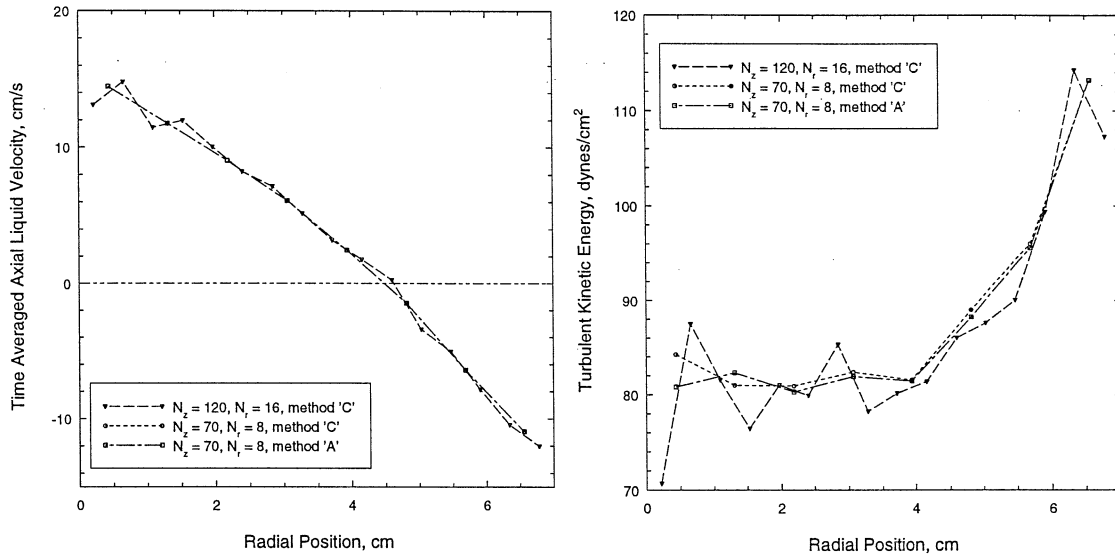
Figure 3.9: Effect of Compartment Discretization on the Circumferentially Averaged (a) Time Averaged Axial Liquid Velocity and (b) Turbulent Kinetic Energy in a 14 cm Diameter Column, $U_g = 2.4$ cm/s, $z = 60$ cm

particle, $v(t, r, \theta, z)$, is measured, and this can be used to compute the Lagrangian statistics such as the Lagrangian auto- and cross-correlation coefficients.

The Lagrangian correlation coefficient for N_{exp} statistically independent experiments is defined by the following equation:

$$R_{pp}(i, j, k, t) = \overline{v'_p(0)v'_p(t)}_{i,j,k} = \frac{1}{N_{exp}} \sum_{n=1}^{N_{exp}} v'_{p,n}(i, j, k, 0)v'_{p,n}(i, j, k, t) \qquad (3.17)$$

where v' is the fluctuating Lagrangian velocity, defined as

$$v'_p(i, j, k, t) = v_p(i, j, k, t) - \overline{v}_p(i, j, k, t) \qquad (3.18)$$

$\overline{v}(i, j, k, t)$ denotes the ensemble average of the velocities measured at time t for experiments initiated in compartment (i, j, k).

Let us consider a compartment with indices (i, j, k). When the particle 'first' enters this compartment a Lagrangian experiment is initiated for this compartment. The

velocity measured for the first particle displacement for this experiment is $v_p(i, j, k, 0)$, where p denotes the component of the velocity. This is the Lagrangian velocity at zero time, $t = 0$, for this experiment initiated in compartment (i, j, k). The velocity of the moving particle is calculated at every subsequent time step, for a certain period of time, which is determined by the time it takes for the correlation to drop to zero. This constitutes one experiment for a given compartment to give $v(i, j, k, t)$. Another experiment for the same compartment is initiated when the particle, again enters the compartment for the 'first' time. 'first' implies that this experiment is statistically independent from the previous experiment, which is ensured when the time interval between this tracer occurrence and the occurrence in which the previous experiment was initiated, is greater than a prescribed limit, T_{lag}. The time T_{lag} is the time required for the two sequences of data to be statistically independent. Typically these $T_{lag} = 20$ time steps. In a similar manner several experiments are initiated and recorded to calculate the auto- and cross-correlation coefficients as defined by Equation 3.17.

The calculation of the Lagrangian correlation coefficients is tedious, since as the particle passes through each compartment, experiments have to be initiated and recorded, for the entire duration of the run and all the compartments in the column. The present algorithm for the computation considers all the compartments simultaneously, and thereby greatly reduces the computational time from the previously existing program (Devanathan 1991). A flowsheet of the algorithm is presented in Appendix B. These Lagrangian correlation coefficients are used to calculate the turbulent eddy diffusivities, details of which are discussed in Chapter 4.

3.8 Wavelet-Based Filtering of CARPT Data

3.8.1 Statistical Nature of γ Radiation

Owing to the quantized nature of the γ photons, the intensity of the radiation emitted by the radioactive tracer particle exhibits continuous fluctuations in time. The

emission of γ photons from a radioactive source is a statistical process which follows a Gaussian distribution, with the mean n_c and standard deviation $\sqrt{n_c}$, where n_c is the number of counts emitted per unit time. The standard error which is defined as the standard deviation/mean counts, is found to vary inversely with the intensity of counts (Tsoulfanidis 1983), as expected in a Gaussian distribution. Ideally three detectors with precise signals are sufficient to locate the particle. However, since the radiation intensity measured at a given sampling instant is not exact and exhibits variations due to the statistical fluctuations, a redundancy of detectors is employed and a weighted least square algorithm is used as a first step in determining the approximate particle position followed by position refinement, as discussed in the previous section. The detector that is the closest to the particle measures the maximum radiation and, therefore, exhibits the least standard error $(1/\sqrt{n_c})$, and is hence weighted the most, and vice-versa. The weighted regression algorithm helps reduce the error in position estimation and results in reasonable estimates of particle positions. However, the fluctuations in the radiation intensity data are still "transmitted" to the instantaneous position data. Figure 3.10 shows a time series of the instantaneous position of a stationary particle estimated over 512 sampling instants. The power spectral density of the instantaneous position data in Figure 3.10 (b), shows the characteristics of white noise, indicating that the statistical fluctuations in the gamma radiation gets transmitted as white noise to the instantaneous position data. The apparent continuous movement of the actually stagnant particle results in the generation of "spurious velocities", i.e., non-zero velocities for a physically stationary particle. For example, Figure 3.11 (a) shows the spurious velocities calculated for a stationary particle in a 14 cm diameter column. Consequently, the instantaneous velocities measured have partial contribution from the statistical fluctuations in the source particle emission. Time or ensemble averaging of the instantaneous velocities in each compartment eliminates these source fluctuations (since the fluctuations have a Gaussian distribution with zero mean). This is reflected in the negligible mean spurious velocities calculated (see Figure 3.11), of the order of 0.1 cm/sec, which are

very small when compared with the actual liquid velocities monitored (10 cm/sec to 60 cm/sec). Hence, the noise in the data does not affect the time averaged velocities. However, the fluctuations (spurious velocities) do contribute to the instantaneous velocities of the particle as it follows the liquid during an experiment, and thereby the fluctuating velocities and the estimated turbulence parameters of the liquid. This causes an over-estimation of the turbulence quantities that are measured.
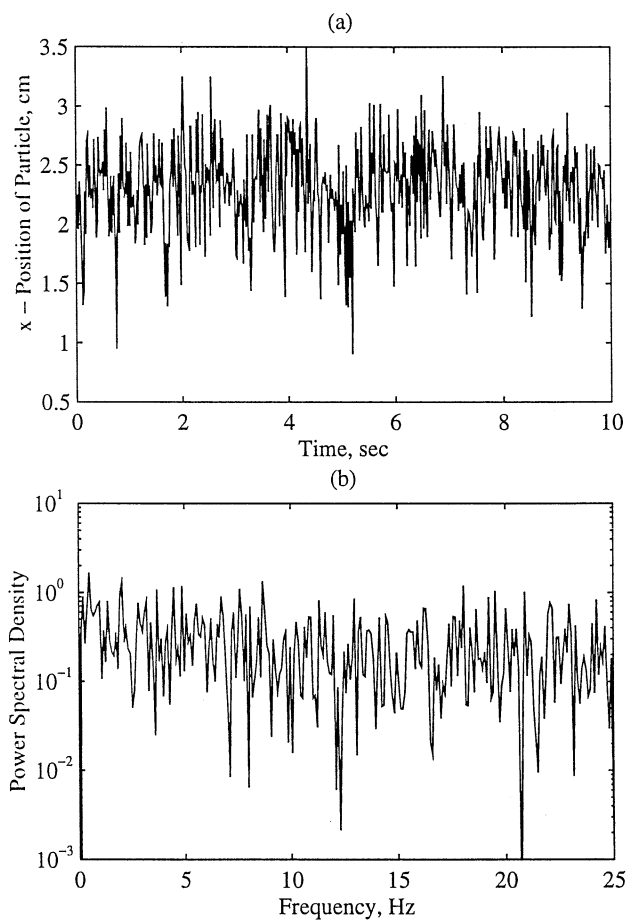

Figure 3.10: Fluctuations in Stationary Particle Position (Taken from Calibration Data in a 14 cm Column, $U_g = 9.6$ cm/s)
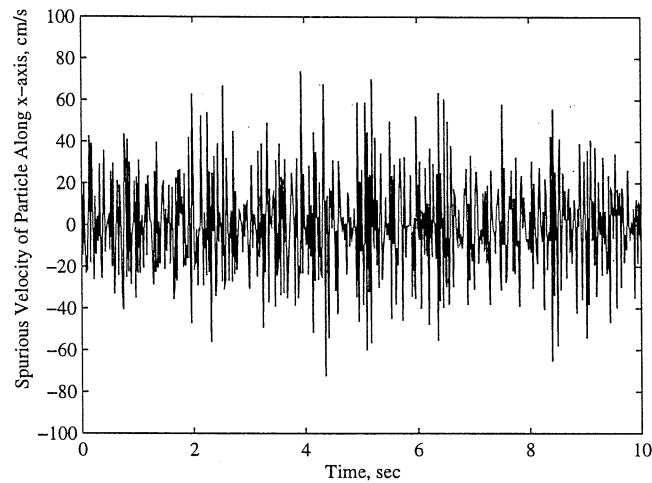
Figure 3.11: Spurious Velocities Calculated from the Data in Figure 3.10, Mean = 0.05 cm/s, rms velocity = 26.4 cm/s

Filtering the White Noise in the Data

In order to obtain better and accurate estimates of the turbulence parameters it is therefore necessary to filter the instantaneous position data and thereby eliminate, or reduce to the best possible extent, the contribution of the spurious velocities to the instantaneous velocities measured.

Traditional Fourier transform filtering (FFT) was first attempted using a third order low-pass Butterworth filter. The cut-off frequency for the low-pass filter was chosen as 20 Hz. An estimate of the cut-off frequency is based on the size of the tracer particle used (2.36 mm). Earlier in this chapter it was shown that the tracer particle, due to it finite size, can follow the liquid well, up to a frequency of about 30 Hz. Results of FFT filtering using a low-pass filter are shown in Figure 3.12 (a). It can be observed from the figure (note the highlighted regions enclosed in boxes) that the resulting filtered signal is unable to capture the sharp peaks of the original signal. As a result, these sharp changes that characterize the flow are removed as noise (refer to bottom part of Figure 3.12 (a)). Increasing the cut-off frequency does not improve the situation as it results in residual high frequency components of the white noise in the signal. Another factor to be considered is that the actual cut-off frequency

required may vary with position in the column as discussed above. This suggests that traditional Fourier transform filtering using a low pass filter is not quite suitable for the purpose of filtering CARPT data, considering the non-stationary nature of the data with its sharp inflections and peaks, which are characteristic of the dynamics of the liquid in the system.

Wavelet transformation, which is a time-frequency based method is a suitable alternative and has the distinct advantage over the Fourier transform technique, as it can be used to analyze nonstationary and localized data, which exhibit varying frequency characteristics with time. This is illustrated in Figure 3.12 (b). The bottom part of the figure shows the noise that is filtered using the wavelet transformation method. This resembles white noise that is present in CARPT data. On the other hand the noise filtered using Fourier transform based filtering contains some characteristic features of the original signal and does not represent white noise.

Wavelet analysis is used as a tool in this work to filter the white noise from CARPT data. In what follows, a brief introduction to wavelet transform and wavelet packet decomposition is given followed by a description of the algorithm used for filtering CARPT data. To demonstrate the suitability of the method for filtering CARPT data and thereby obtaining a more reliable estimate of the fluid dynamic parameters, an experiment has been conducted with a controlled motion of the radioactive tracer particle. This enables *a priori* knowledge of the trajectory of the particle and provides a reference against which the results from CARPT experiments subject to wavelet packet filtering can be compared. A quantitative estimate of the errors involved in the estimation of the particle position is obtained and the extent to which the intrinsic noise in the data is removed is demonstrated. Thereafter, a few typical bubble column results after wavelet filtering are presented and compared with the results obtained prior to filtering.
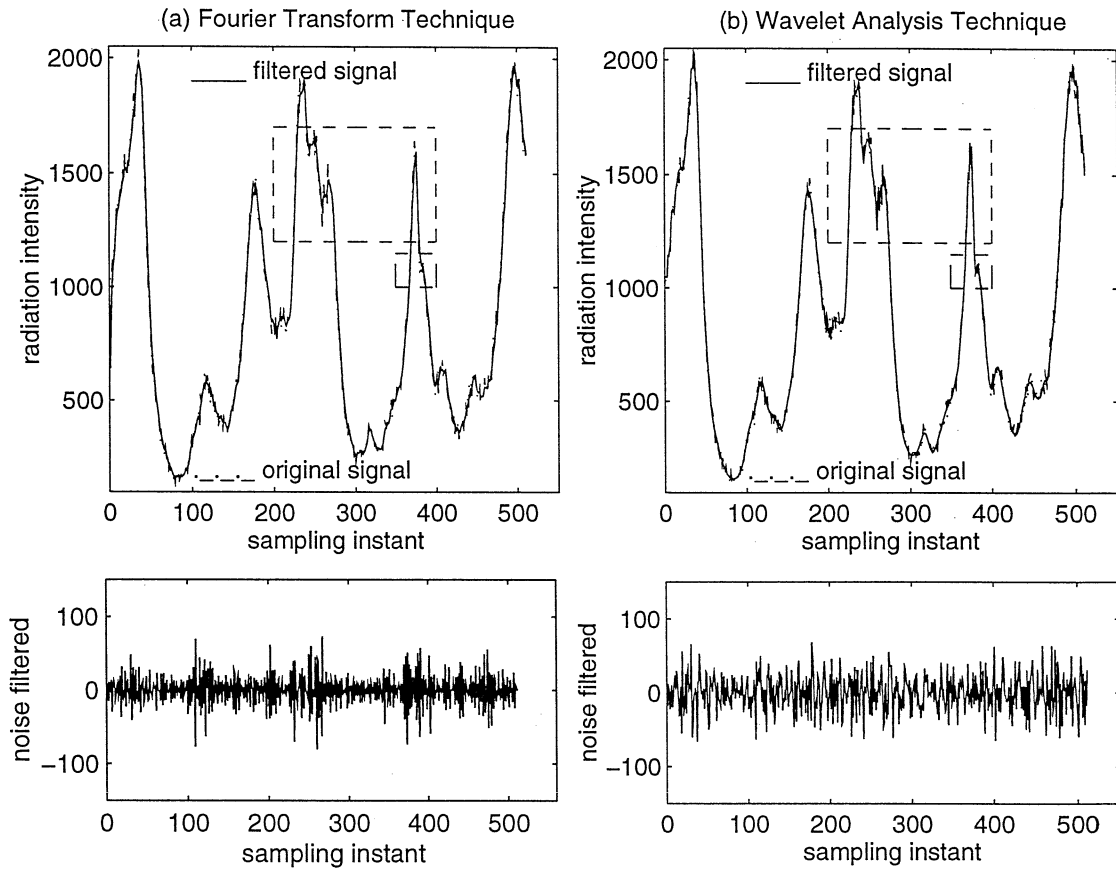
Figure 3.12: Comparison of Classical Fourier Transform and Wavelet Analysis techniques for filtering CARPT data

3.8.2 Wavelet Analysis

Some basic concepts of wavelet analysis

Wavelet transform maps a time domain signal onto a time-scale plane (scale is the inverse of frequency). The transformation is performed using a family of wavelets, $\psi_{a,b}(t)$, generated by the dilation and translation of a function $\psi(t)$, called the basis or mother wavelet, i.e.,

$$\psi_{a,b}(t) = \mid a \mid^{-1/2} \psi(\frac{t-b}{a}), \quad a, b \in R \tag{3.19}$$

is a family of wavelets, where a and b are the dilation and translation parameters, respectively. These functions have prescribed smoothness, are well localized in time and frequency and form a well behaved basis (Daubechies 1988). Each wavelet has a specific time-frequency localization. Parameters a and b determine the compromise between time and frequency. For instance, wavelets of high frequency, i.e., large a, are narrow in time, while wavelets of low frequency are broad in time. As a result wavelets are able to "zoom-in" on shortlived high frequency phenomena, and "zoom-out" on longlived low frequency phenomena. Wavelet transformations, thus work well for cases of filtering non-stationary signals clouded with white noise, and are still able to capture the sudden changes in the signal. There are a number of wavelets with different properties available in the literature, for example, Chui-Wang wavelets, Coiflets, Daubechies wavelets, etc. (for example, see Chui 1992; Palavajjhala et al. 1994). In this investigation Daubechies orthonormal wavelets (Daubechies 1988) are used.

Wavelets are broadly classified as continuous wavelets and discrete wavelets. The term *wavelet transform* is very generic and can be categorized as continuous wavelet transforms and discrete wavelet transforms which use continuous wavelets and discrete wavelets, respectively. The theory regarding wavelet transforms and various aspects of wavelet analysis and their applications can be found in Chui (1992), Daubechies (1992), Wickerhauser (1991) and Joseph and Motard (1995). In what follows the aspects of wavelet analysis that are used in this work is described. A brief introduction along with the underlying basic concepts to discrete wavelet transforms (DWT) and wavelet packet decomposition (WPD) is first presented.

Discrete wavelet transforms involve the projection of a data set onto discrete wavelets to give discrete wavelet coefficients. This is represented as :

$$\langle f, \psi_{m,n} \rangle = 2^{-m/2} \int_{-\infty}^{\infty} f(t)\psi(2^{-m}t - n)dt \qquad (3.20)$$

where the dilation and translation parameters, a and b, in Equation 3.19 are discretized respectively as $a = a_0^m$, $b = nb_0a_0^m$ (a_0 (=2) and b_0 (=1) are constants).

The inner product defined in Equation 3.20 for various values of m, n are called the discrete wavelet coefficients. The reconstruction of $f(t)$ from these coefficients for orthogonal wavelets is given by

$$f(t) = \sum_{m,n \in Z} \psi_{m,n}(t) \langle f(t), \psi_{m,n}(t) \rangle \tag{3.21}$$

DWT is a special case of Wavelet Packet Decomposition (WPD). In WPD, a library of wavelet packets are generated, from which a variety of bases can be extracted to represent the signal. The construction of wavelet packets can be represented in a hierarchy as shown in Figure 3.13. Using two filters, H, a low-pass filter and G, a band-pass filter, the entire library of wavelet packets is generated using a recursive scheme (Wickerhauser 1991) as follows:

$$\psi_0 \overset{\text{def}}{=} H\psi_0; \quad \int \psi(t)dt = 1 \tag{3.22}$$

$$\psi_{2f} \overset{\text{def}}{=} H\psi_f; \quad \psi_{2f} = \sqrt{2} \sum_j h(j)\psi_f(2t - j) \tag{3.23}$$

$$\psi_{2f+1} \overset{\text{def}}{=} G\psi_f; \quad \psi_{2f+1} = \sqrt{2} \sum_j g(j)\psi_f(2t - j) \tag{3.24}$$

$$\psi_{s,f,p} = \psi_f(p - 2^{-s}t) \tag{3.25}$$

where s, f, p denote the scale, frequency and position indices, respectively. h and g are the filter coefficients associated with the low-pass and band-pass filters H and G, which are characteristic of the wavelet function used. The nature of the wavelet packets generated depend on h and g. There are a variety of wavelets available, of which Daubechies' (1988) orthonormal, compactly supported wavelets are most popular.
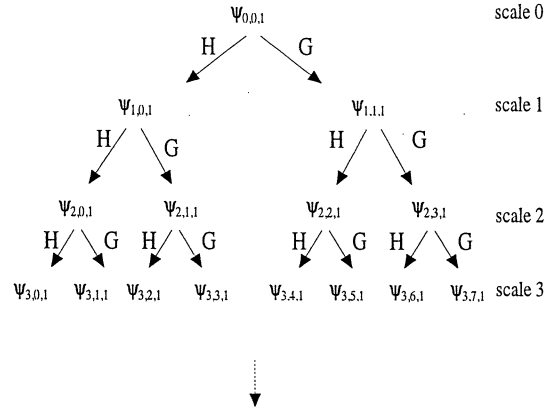
$\Psi_{0,0,1}$ scale 0

H / \ G

$\Psi_{1,0,1}$ $\Psi_{1,1,1}$ scale 1

H / \ G   H / \ G

$\Psi_{2,0,1}$ $\Psi_{2,1,1}$ $\Psi_{2,2,1}$ $\Psi_{2,3,1}$ scale 2

H / \ G   H / \ G   H / \ G   H / \ G

$\Psi_{3,0,1}$ $\Psi_{3,1,1}$ $\Psi_{3,2,1}$ $\Psi_{3,3,1}$ $\Psi_{3,4,1}$ $\Psi_{3,5,1}$ $\Psi_{3,6,1}$ $\Psi_{3,7,1}$ scale 3

Figure 3.13: Hierarchy of Wavelet Packets in Wavelet Packet Decomposition

The decomposition of the signal onto these wavelet packets constitutes WPD. As in the case of DWT, the wavelet packet coefficients are given by :

$$\lambda_{s,f,p} = \langle f, \psi_{s,f,p} \rangle = 2^{-s/2} \int f(t) \psi_f(p - 2^{-s}t) dt \qquad (3.26)$$

where λ is the wavelet packet coefficient. Alternatively,

$$\lambda_{s+1,2f,p} = H\lambda_{s,f,p} \qquad (3.27)$$

$$\lambda_{s+1,2f+1,p} = G\lambda_{s,f,p} \qquad (3.28)$$

The resulting library of wavelet packet coefficients contains redundant information from which a variety of bases can be chosen. The best representation is the one that has the least number of significant coefficients. There are several ways of identifying a best basis representation using some type of information cost. The most appealing is the one that has the least information entropy. An additive measure of entropy (Coifman and Wickerhauser 1992) is defined as

$$e = -\sum_i |\lambda_i|^2 \ln |\lambda_i|^2 \qquad (3.29)$$

where λ_i are the wavelet packet coefficients. The more randomness in the signal, the greater its entropy, and therefore the greater the number of coefficients required to represent the signal accurately which means larger information cost. This concept has found applications in denoising a noisy signal, data compression and speech scrambling, among others. This can be illustrated by the following example

Consider a signal such as a sinusoidal wave, $f_s = \sin(10\pi t)$, at a frequency of 10 Hz, with an amplitude of 1, such that the signal energy $(\sum_i^N f_s(i)^2) = 500$ units, where $N = 1024$ is the length of the signal. This periodic signal represents a coherent structure. Using the wavelet packet decomposition and the best basis representation, this signal can be well represented with a minimum of 90 wavelet packet coefficients. On the other hand, if one considers a signal characterizing white noise, f_n, with the same energy level of 500, a best basis representation of this white noise requires at least 750 coefficients (largest coefficient is 1.8 in magnitude, as opposed to 28 for the sinusoidal wave). This illustrates the difference between a coherent signal, which can be represented by a few large wavelet packet coefficients, and white noise which is an incoherent signal and can only be represented by a large number of small wavelet packet coefficients.

It is of interest to apply the wavelet packet decomposition and the best basis algorithm in denoising or filtering of noisy signals. The idea is to extract coherent parts present in the signal, i.e. the signal features with good time-frequency localization, by adopting the method of adapted waveform denoising proposed by Coifman et al. (1993). The signal is first transformed to wavelet packet coefficients from which the best basis coefficients are selected. A part of the signal represented by a few largest coefficients is used to extract a coherent part of the signal. The remaining incoherent part is decomposed several times to extract all the coherent parts remaining in it. All the individual coherent parts, thus extracted, are superimposed to give the filtered signal. The incoherent part remaining at the end is rejected as noise. The advantage of the algorithm is that exact characterization of the process is not required. This

method is similar to the Matching Pursuit Algorithm discussed by Mallat and Zhong (1992).

In the present work, the waveform denoising algorithm (Coifman et al. 1993) described above is adopted with some modifications. Since the signal to noise ratio of the data is high, 95:5 , i.e., the energy level of the noise in the signal is low, a suitable threshold for the magnitude of the wavelet packet coefficients is chosen, by which a large number of coefficients with magnitudes below the threshold are set to zero. These coefficients, having low energy, are considered to represent the noise in the signal and are thereby removed.

3.8.3 Wavelet Packet Filtering of CARPT experimental data

The noise present in the radiation intensity data, gets transmitted to the estimated particle position data in Cartesian coordinates, $P(x, y, z)$, as shown earlier. It is found that the noise in each coordinate is white noise, uncorrelated with each other. Filtering can be applied either to the radiation intensity data, measured by each detector following which the particle position is estimated, or directly to the instantaneous position data. Since the results from the two methods are equivalent (Figure 3.14), the latter approach of filtering the position data is chosen as it is more efficient in computing resources.

Wavelet packet decomposition using Daubechies' (1988) orthonormal, nearly symmetric wavelets is employed for this analysis. The algorithm for analysis and filtering of the data is explained below. The original signal (CARPT instantaneous position data) is divided into data sets of length $N = 2^L$; $L = 10$, $N = 1024$. For each data set of length N sampled at a constant frequency, the wavelet packet decomposition, described earlier, is performed and subsequently the best basis representation, based on minimizing the entropy of the coefficients (Equation 3.29), is obtained. The wavelet packet coefficients (wpc) in the chosen best basis are arranged in descending order of amplitude ($|wpc|$). The fraction of the coefficients corresponding to those with the largest magnitude, i.e., the first few significant coefficients,
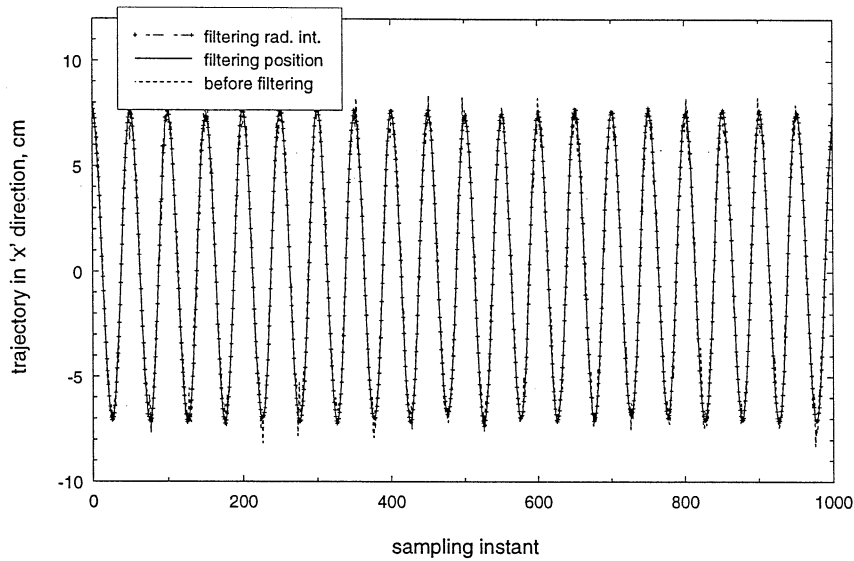
Figure 3.14: Comparison of Results Obtained from Filtering the Intensity Data versus Position Data

represent the coherent part of the signal while the remaining weak coefficients, of low magnitude depict the noise. The energy level of the noise in the data is very low and constitutes typically less than 5 % of the total signal energy. This information is obtained by analysis of the CARPT calibration data, as described below.

The objective of the wavelet filtering is to extract only the coherent part of the signal leaving out the noise. This is achieved by selecting a signal threshold for the wavelet packet coefficients, 'st'. All the coefficients below this threshold are set to zero. Only the fraction of coefficients with magnitudes larger than the set threshold are retained, re-ordered and reconstructed to yield the filtered signal. The filtering algorithm hence requires a predetermined value for the signal threshold, 'st'. The choice of 'st' depends on the extent of noise in the data, $x(t)$, $y(t)$ and $z(t)$. An initial estimate of st is obtained using the experimental data for a stationary particle measured during the calibration. Fine tuning of 'st' is then done, to ensure that the noise filtered from the data satisfies the characteristics of white noise. The power spectral density is used as the basis for verification. White noise has a uniform distribution of energy over all the frequencies (maximum is the Nyquist frequency) sampled. The value of 'st' is adjusted such that the filtered noise shows a uniform

power spectrum, with no peaks (the presence of peaks is an indication that a part of the actual signal is removed). The process of tuning is done with several randomly chosen data sets to arrive at the final value of st for the data, which is then used for filtering the instantaneous position data. The initial estimates of 'st', from the calibration data, are usually slightly higher than the final tuned value. The values of st can vary for x, y and z. Typically st is anywhere between 0.7 to 2.0, increasing with column diameter, and is found to be dependent on the operating conditions as well. At very high gas velocities, the effect of the fluctuations from the bubbles seems to increase the noise in the data. The filtering results are, however, insensitive to minor variations in the threshold value ($\pm$ 0.05 to 0.15).

Filtering using the above described algorithm ensures maximum extent of reduction of the noise in the data, resulting in a smoother version of the signal and simultaneously helps in retaining the sharp features arising from the nature of the flow in the system. The algorithm is implemented using the commercial software WAVBOX[1] on MATLAB. The wavelet toolbox provides the necessary subroutines for construction of wavelets, WPD and reconstruction of the signal.

In order to verify the applicability and effectiveness of the algorithm for filtering the noise from the experimental data, the algorithm is tested with data produced from experiments for a controlled motion of the tracer particle.

3.8.4 Experiments with the Controlled Movement of the Particle

Experimental Setup

The experimental setup principally consists of two motors, a screw conveyor and a plate as shown in Figure 3.15. Motor I is secured at the bottom of the structure and is geared to a screw conveyor that is positioned vertically. The screw conveyor supports a vertical frame on top of which the plate is mounted. The shaft of motor II, which is

---

[1]WAVBOX is a wavelet toolbox (commercial software) written by Taswell for a MATLAB environment

fixed to the top of the plate, is connected to a smooth, circular disc. The radioactive particle to be tracked is fixed to the tip of a thin Plexiglas rod attached to the disc. Operation of motor II causes the particle to move in a circular motion. The maximum frequency of motion is 3 Hz. The distance of the particle from the axis varies from 7 to 8 cm. Simultaneously motor I causes the plate held to the frame to move
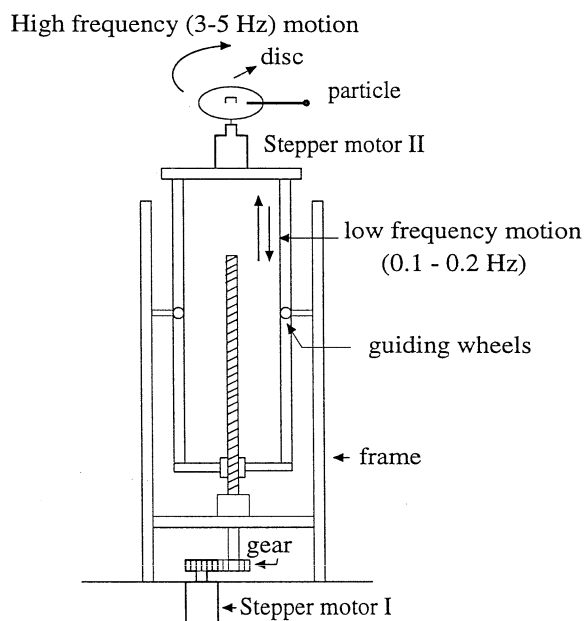

Figure 3.15: Experimental setup for controlled motion of particle

vertically in "up and down" motion (with frequencies of the order of 0.1 Hz). The maximum vertical distance traversed by the particle is 6.4 cm. By this arrangement the particle is made to move in a spiraling 3D motion, with high (3 Hz) and low (0.2 Hz) frequencies. The two motors are driven by microprocessors, which are interfaced with a personal computer. This arrangement ensures the precision with which the particle moves. A trolley system with guiding wheels provided for guiding the frame helps in minimizing the vibration of the setup. The entire structure is supported on the plenum centered between the detector supports (not shown in figure). Sixteen strategically positioned detectors are used for detecting the γ radiation from the source particle. Calibration is first performed using various particle positions that cover the entire range of experimental runs. Subsequently the experimental runs are

performed. In each run, the speed of the two motors is varied, thereby varying the velocity of the particle. Six such runs were performed.

Experimental Results

The details of the experimental runs carried out are shown in Table 3.4. The experiments are conducted in air. Motor I moves the particle in a linear vertical motion, i.e. along the z axis in Cartesian coordinates. Motor II moves the particle in a horizontal two dimensional circular trajectory, i.e. in a $x - y$ plane. A parametric representation of the trajectory of the tracer particle is given as:

$$x_t = x_c + r_p cos(\theta_0 \frac{\pi}{180}) + r_p cos(2\pi \omega_2 t) \tag{3.30}$$

$$y_t = y_c + r_p sin(\theta_0 \frac{\pi}{180.0}) + r_p sin(2\pi \omega_2 t) \tag{3.31}$$

$$z_t = z_0 + \omega_1 t \tag{3.32}$$

where x_c and y_c are biases in position due to experimental constraints. r_p is the radius of curvature which the particle traverses. θ_0 is the initial angular position of the particle. ω_2 is the frequency of rotation of motor I. ω_1 gives the displacement of the particle per unit time and is related to the rpm of motor I. Motor I is programmed to move 800 steps, first in the clockwise direction, followed by the counter clockwise direction. This periodic motion is repeated several times. 125 steps in the clockwise direction is equivalent to 1 cm. This induces a frequency of about 0.1 Hz in the z direction of motion. Based on the trajectories, the existing Lagrangian velocities v_{x_t}, v_{y_t} and v_{z_t} are calculated.

The instantaneous position data x_p, y_p and z_p resulting from CARPT experiments for the controlled motion of the particle are subject to wavelet packet filtering as discussed in the previous section ($st_x = 0.9$ to 1.1, $st_y = 0.9$ to 1.1, $st_z = 1.0$ to 1.3), yielding filtered results x_f, y_f and z_f. Thereby the particle velocities from CARPT

Table 3.4: Details of Experimental Runs for Controlled Motion of Particle

Run No.	r_p cm	θ_0, deg	ω_1 cm/sec	z_0 cm	z_f cm	ω_2 1/sec
Run 1	6.964	315	2.0	112.21	118.61	2.75
Run 2	7.989	270	2.0	112.81	119.41	0.00
Run 3	7.180	315	2.0	112.21	118.61	1.00
Run 4	7.180	315	2.0	112.21	118.61	2.00
Run 5	7.180	315	2.0	112.21	118.61	2.75
Run 6	7.989	315	2.0	112.21	118.61	1.50

measurements (sampling frequency is 50 Hz) before filtering, v_{x_p}, v_{y_p} and v_{z_p}, and after filtering, v_{x_f}, v_{y_f} v_{z_f}, are obtained. The results are analyzed by comparing the magnitude of the error in positions and velocities in each direction. For this purpose the root mean square (rms) error is defined as

$$\text{rms error in position } \quad j = \sqrt{\frac{\sum_i^N (j - j_t)^2}{N}} \quad j = x, y, z \qquad (3.33)$$

$$\text{rms error in velocity } \quad v_j = \sqrt{\frac{\sum_i^N (v_j - v_{j_t})^2}{N}} \quad j = x, y, z \qquad (3.34)$$

where N is the number of samples considered. The error in velocity gives the spurious velocity of the particle.

Figure 3.16 (a) shows the actual trajectory y_t for a period of 10 sec, for Run 5 reported in Table 3.4. Figure 3.16 (b) is a comparison of the error in estimating the successive y positions of the particle. Figures 3.17, 3.18 and 3.19 show the velocities of the particle in all the three directions along with the errors before and after filtering. The particle trajectory projected on the horizontal x - y plane is essentially a circle. Such a trajectory for two cycle periods is shown in Figure 3.20 for Run 5, before and after filtering, along with the actual trajectory. A summary of the results for the

entire set of runs is presented in Table 3.5 which reports the errors in position x, y and z, and spurious rms velocities, before and after filtering.
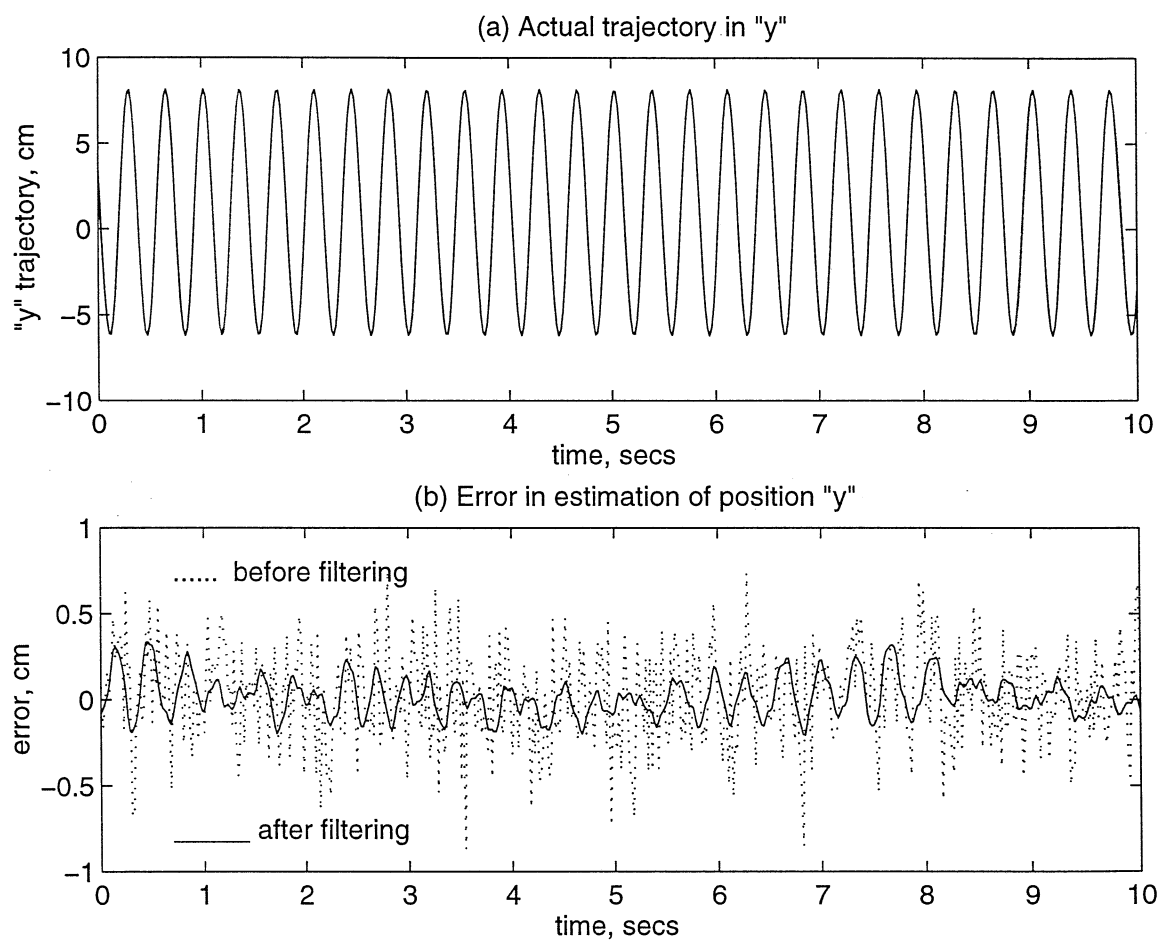

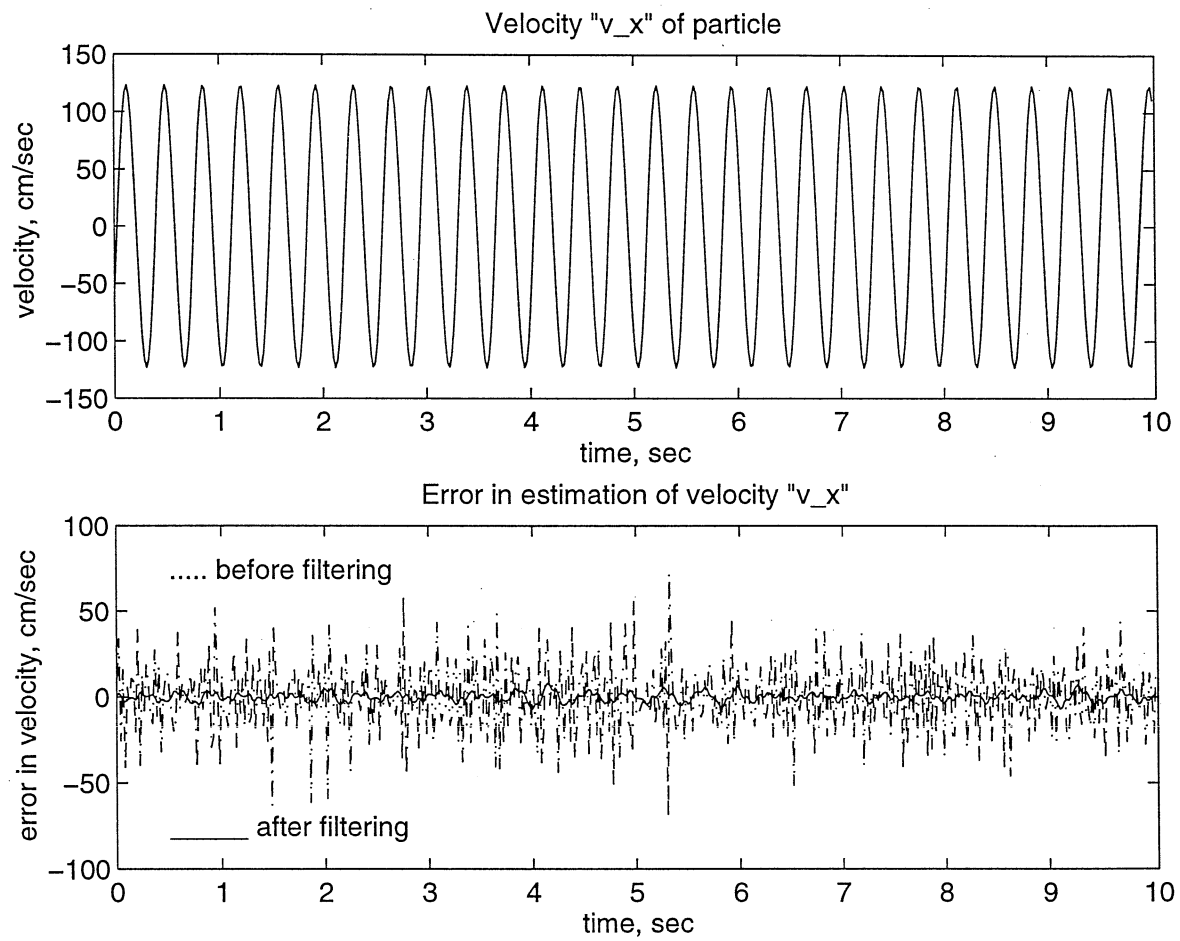Figure 3.16: Results for RUN 5 : trajectory y of particle

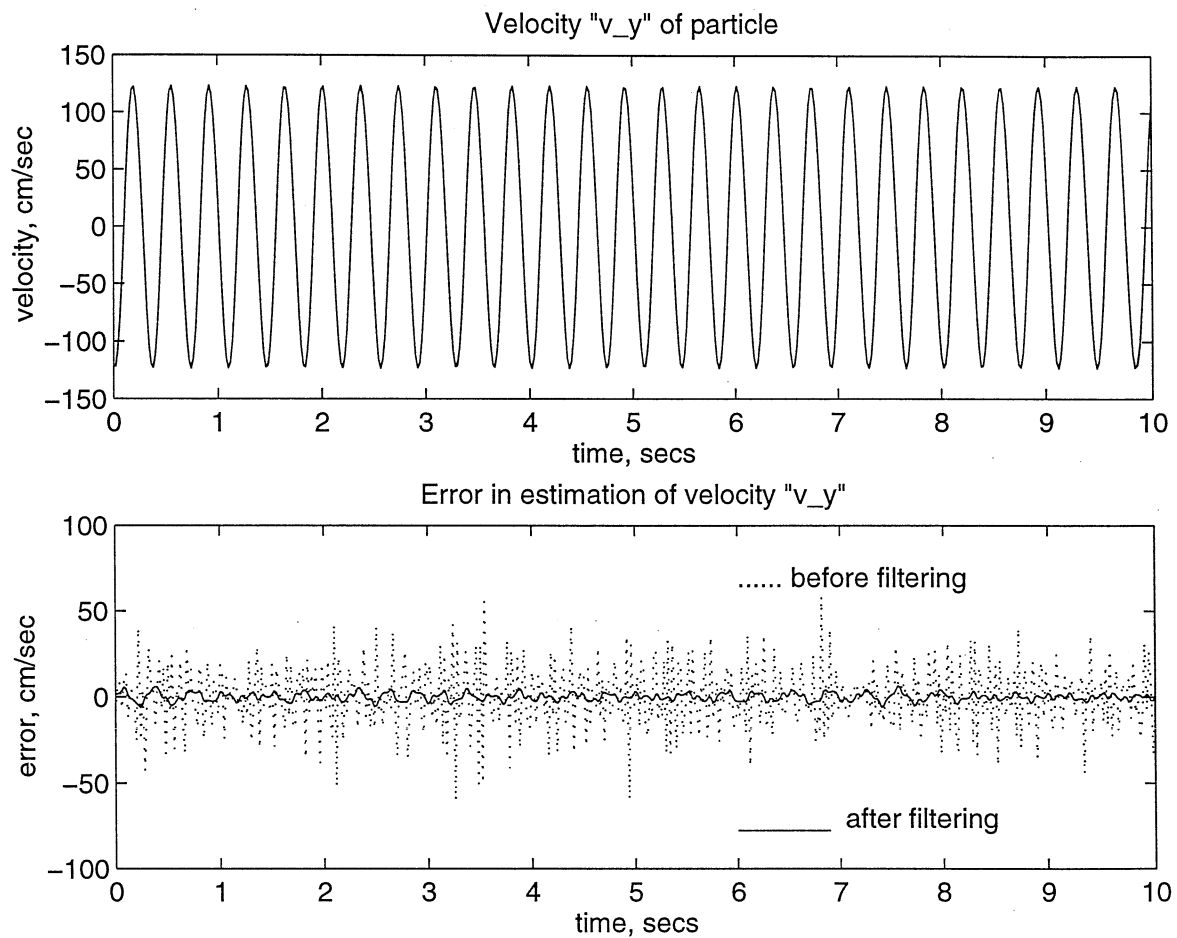Figure 3.17: Results for RUN 5 : Velocity v_x and error in estimation of velocity of particle

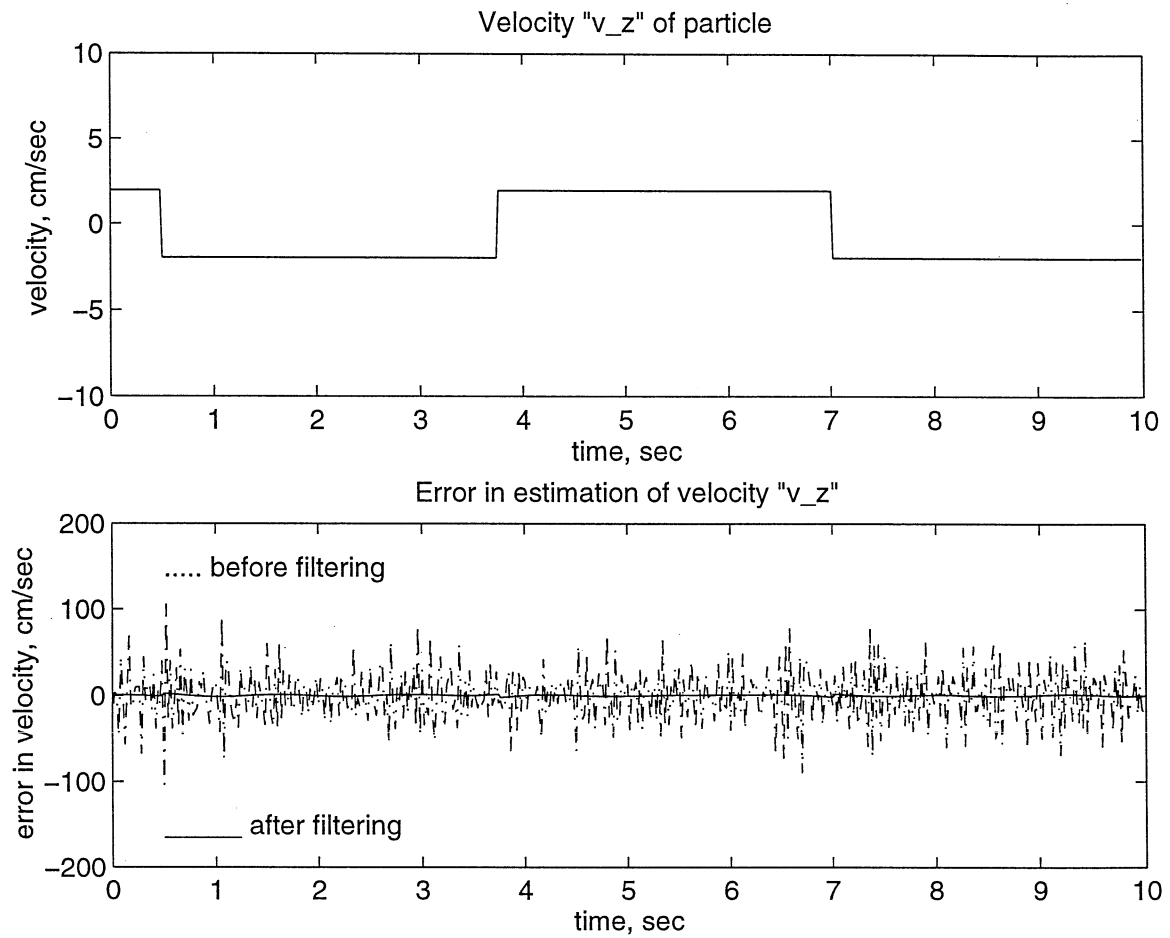Figure 3.18: Results for RUN 5 : Velocity v_y and error in estimation of velocity of particle

Figure 3.19: Results for RUN 5 : Velocity v_z and error in estimation of velocity of particle

It is evident by examining the results, that there is significant improvement in the accuracy of estimation of both the positions and velocities of the moving particle. The residual error (spurious rms velocities) after filtering the data is 2-5 cm/sec. This represents an average of 75% (maximum of 95 %) reduction in the level of noise in the data. With regard to the magnitude of the rms fluctuating velocities of the liquid in bubble columns, which are an order of magnitude higher, the reduction in error is considered substantial.

The experiment for the controlled motion of the tracer particle thus provides a basis for the validation of the CARPT technique in estimating the trajectory and velocities of the moving particle, using the wavelet analysis technique for filtering the intrinsic noise in the instantaneous position data.
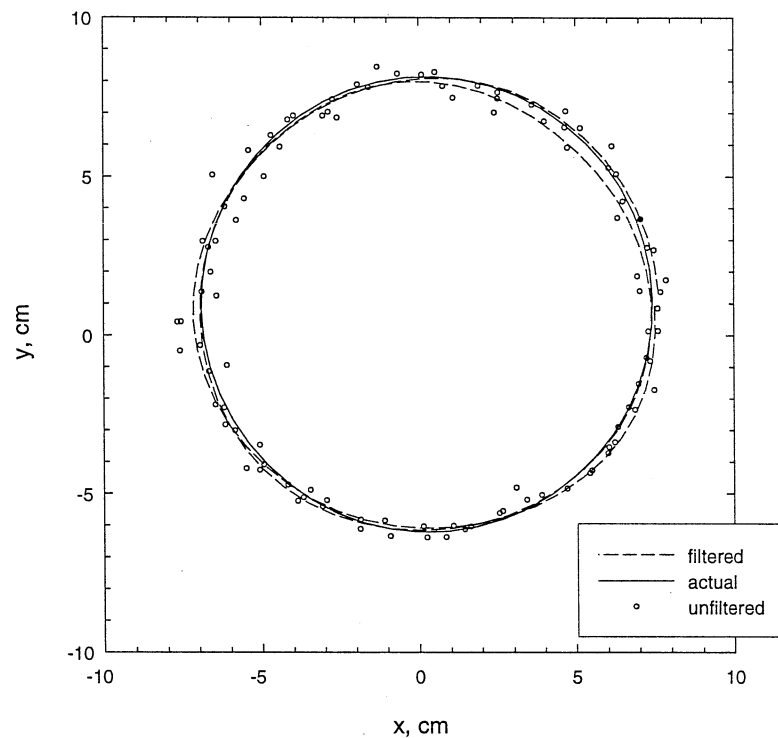
Figure 3.20: Circular Trajectory of Particle for Run 3

Due to experimental constraints, it has been possible to perform experiments with the controlled motion of the particle only at fixed frequencies. It is also of

Table 3.5: Errors in Estimation of Particle Position (cm) and Velocity (cm/sec)

Run	Dir-	Error in Position, cm				Error in Velocity, cm/sec	
	ect-	Before Filtering		After Filtering		Bef. Filt.	Aft. Filt.
No.	ion	rms	min/max	rms	min/max	rms	rms
Run 1	x	0.32	-1.17,1.12	0.19	-0.7,0.6	20.5	4.16
	y	0.36	-.15, 1.2	0.26	-0.75, 0.8	20.01	4.66
	z	0.49	-1.7,1.4	0.25	-0.7,0.74	30.36	1.68
Run 2	x	0.31	-0.97,1.03	0.03	-0.04,0.03	16.99	0.07
	y	0.28	-1.10,1.15	0.007	-0.01, 0.02	17.94	0.04
	z	0.40	-1.3,1.03	0.25	-0.79, 0.5	24.29	1.05
Run 3	x	0.32	-1.16,1.13	0.21	-0.7,0.9	19.3	3.2
	y	0.31	-1.2,1.2	0.21	-0.85,0.8	18.0	3.6
	z	0.47	-1.5, 1.75	0.17	-0.9, 0.6	28.9	1.34
Run 4	x	0.32	-1.08,1.12	0.22	-0.75,0.86	19.5	4.8
	y	0.32	-1.5,1.25	0.23	-0.7,0.75	19.0	4.5
	z	0.46	-1.4,1.4	0.21	-0.65,0.61	29.0	1.38
Run 5	x	0.3	-1.11,1.32	0.19	-0.9,0.66	20.2	5.4
	y	0.29	-0.89,0.9	0.16	-0.61,0.65	18.7	3.8
	z	0.47	-1.6,1.4	0.22	-0.87,0.72	29.2	1.56
Run 6	x	0.31	-1.16,1.08	0.21	-0.8,1.0	19.78	4.18
	y	0.28	-1.14,1.11	0.14	-0.84, 0.82	18.69	3.51
	z	0.37	-1.09,1.21	0.20	-0.86, 0.72	25.73	1.48

interest to illustrate the capability of the present filtering algorithm for the case of time series data containing varying frequencies, which are characteristic of the instantaneous position data measured from bubble column experiment. This is done by numerically generating a time series with varying frequency components, and superimposing on this signal white noise that is characteristic of the fluctuations present in the instantaneous position data from CARPT. The signal considered for this purpose is defined by the following equation:

$$f_{ch}(t) = A_n(\sin(\frac{\pi t^2}{6}) + \sin(\frac{\pi t^3}{200}))$$ (3.35)

The two terms on the right hand side of Equation 3.35 are referred to as 'chirp' signals, (the first is a linear 'chirp' and the second is a quadratic 'chirp'). The square and cubic variation of time in the first and second term, respectively, induces a frequency variation in the time series $f(t)$. White noise, $n(t)$, that is typical of the noise present in CARPT data is superimposed on $f(t)$ resulting in a noisy signal, $f_n(t)$.

$$f_n(t) = f_{ch}(t) + n(t) \qquad \sigma_n^2 = 0.1 \qquad (3.36)$$

The wavelet filtering algorithm is applied to $f_n(t)$, using a threshold of $st=1.0$, which is arrived at by studying the wavelet packet decomposition of the noise, $n(t)$, as described earlier. The noisy signal and the filtered signal are shown in Figure 3.21.
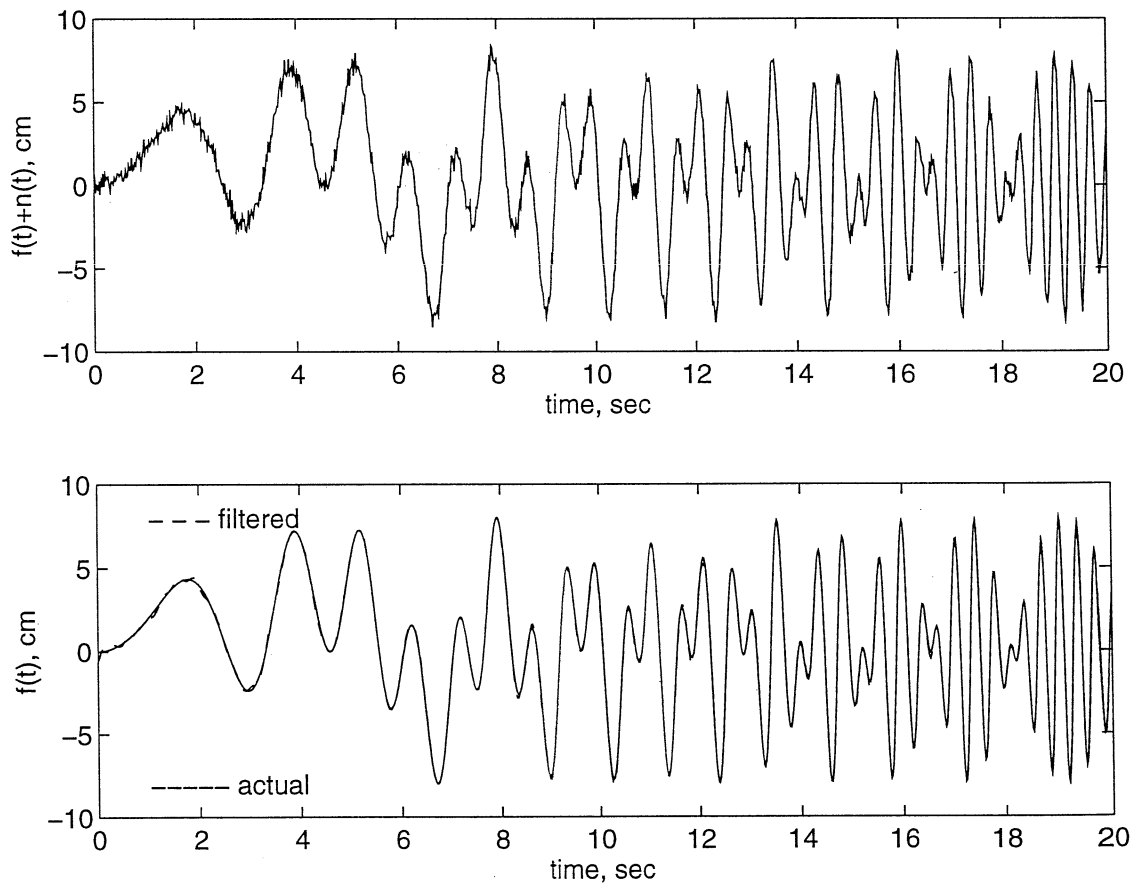
Figure 3.21: Filtering of the Numerically Generated Noisy 'Chirp' Signal

The root mean square error in the signal is reduced from 0.44 cm to 0.109 cm after filtering. Effects of filtering are apparent in Figure 3.22 which shows the velocity computed by time differencing the signal. The root mean square error in the velocity is reduced from 19.9 cm/s, before filtering, to 3.19 cm/s after filtering. This demonstrates the suitability of the proposed wavelet-based filtering algorithm for filtering signals similar to CARPT data, with varying low and high frequency components.
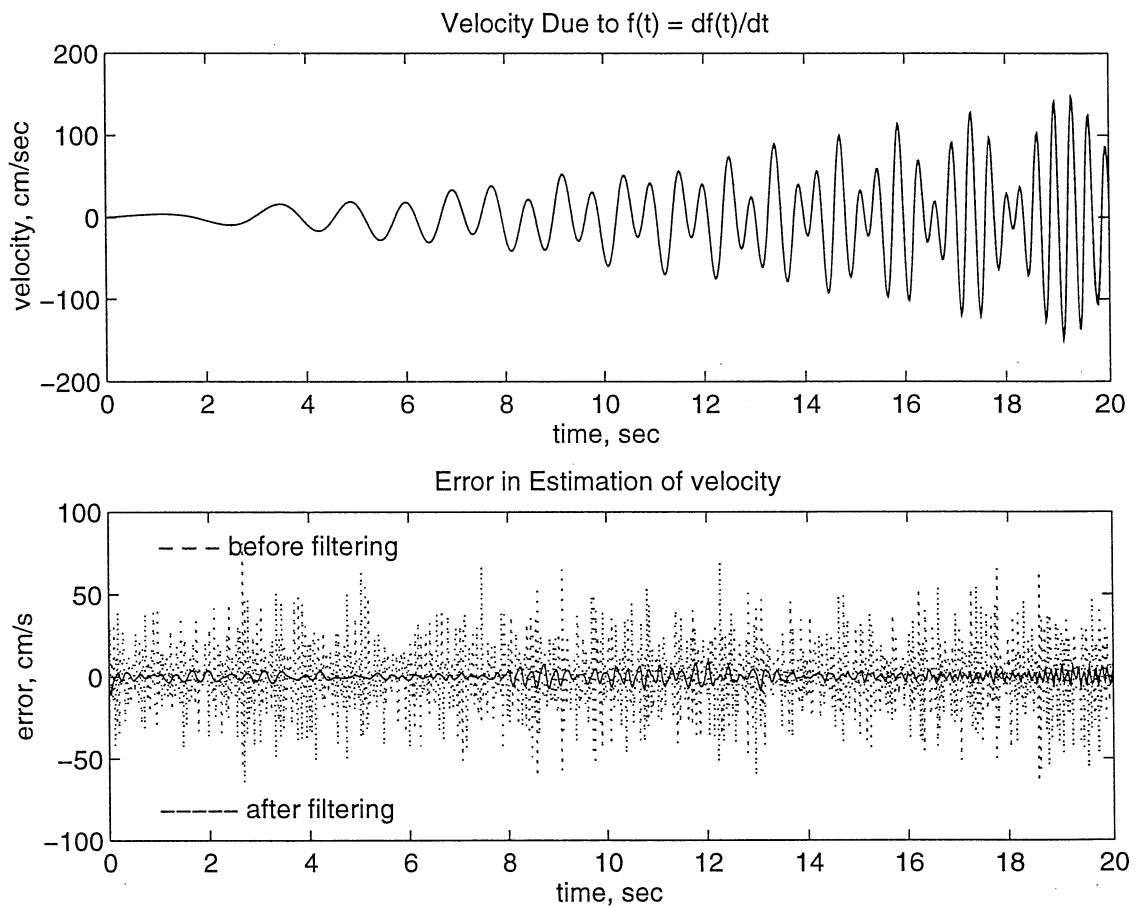
Figure 3.22: Error in the Velocities Computed by Differentiation of the Chirp

3.8.5 Wavelet Filtering of CARPT Data in Bubble Columns

The wavelet filtering algorithm is applied to all the bubble column experimental data obtained as part of this work. The thresholds required for performing the filtering are obtained using the procedure described in the earlier section ('st' varies from 0.7 to 1.0 for a 14 cm diameter column; 0.8 to 1.2 for a 19 cm diameter column; 1.4 to 1.8 for a 44 cm diameter column) .

A few typical results are presented comparing the effects of filtering on the various fluid dynamic parameters. Figure 3.23 shows the comparison of the time averaged axial liquid velocity in a 14 cm diameter column, at two superficial gas velocities. The results before and after filtering are nearly identical. This is expected, as it is known that the spurious velocities get averaged out in the process of time averaging, and therefore do not affect the mean velocities. On the other hand there is a significant reduction in the magnitude of the turbulent normal stresses as seen in Figures 3.24 and 3.25 for superficial gas velocities of 2.4 cm/s and 9.6 cm/s, respectively, in a 14 cm diameter column. Figure 3.24 for the lower gas velocity shows a lower level of noise, as discussed earlier.
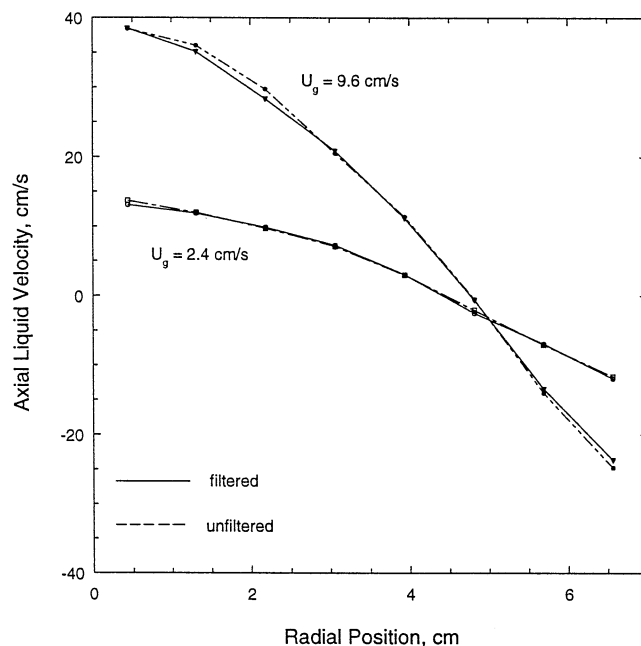
Figure 3.23: Comparison of the Time Averaged Liquid Velocities Before and After Filtering in a 14 cm Column
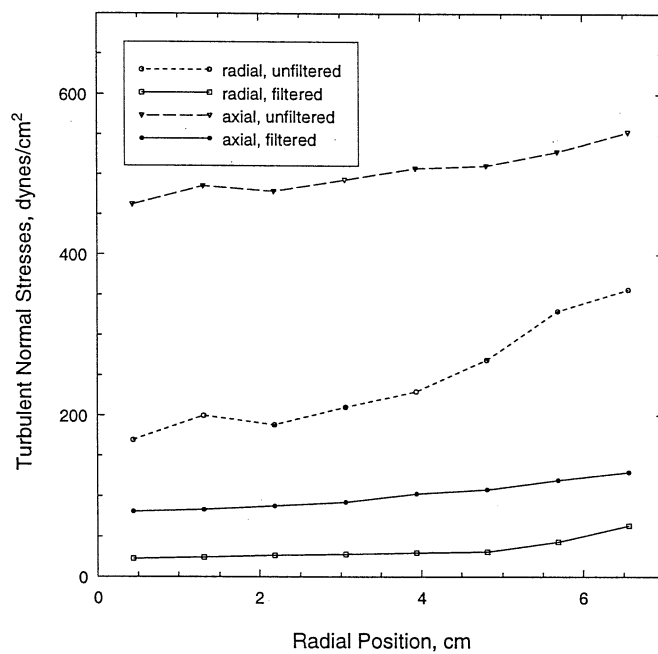
Figure 3.24: Comparison of the Turbulent Normal Stresses Before and After Filtering, Col. Dia. 14 cm, $U_g = 2.4$ cm/s
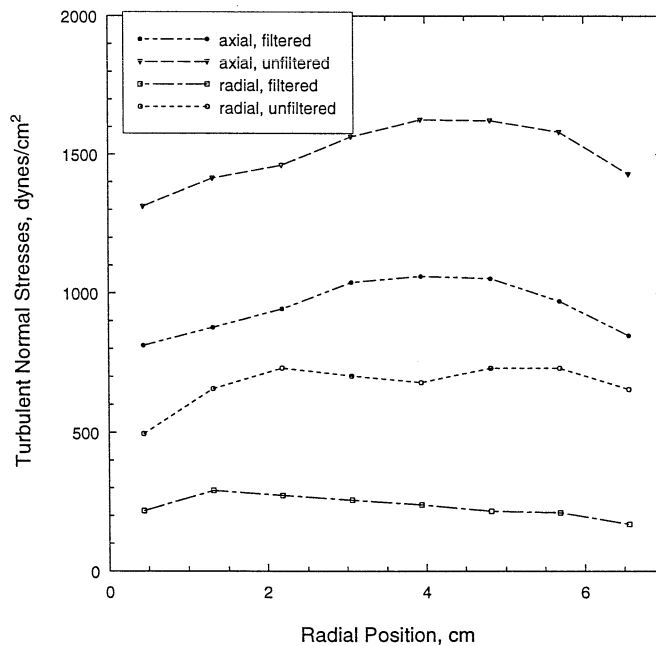

Figure 3.25: Comparison of the Turbulent Normal Stresses Before and After Filtering, Col. Dia. 14 cm, $U_g = 9.6$ cm/s

Figure 3.26 shows the effects of filtering on the turbulent shear stress in a 14 cm column at gas velocities of 2.4 cm/s and 9.6 cm/s. As opposed to the normal stresses and turbulent kinetic energy, the effect of filtering cannot be judged based on the reduction in the magnitude of the shear stress. The reason for this is because the shear stress measurement involves the cross-correlation of the radial and axial turbulent velocities. Unlike the results for the normal stresses, the presence of noise in the data causes the shear stress calculated to oscillate between positive and negative values (due to the cross-correlation) and does not specifically result in an increase in the magnitude of the quantity. This is clearly illustrated in the positive and negative values of the shear stress calculated from the unfiltered data, while for the filtered data the results show expected trends.
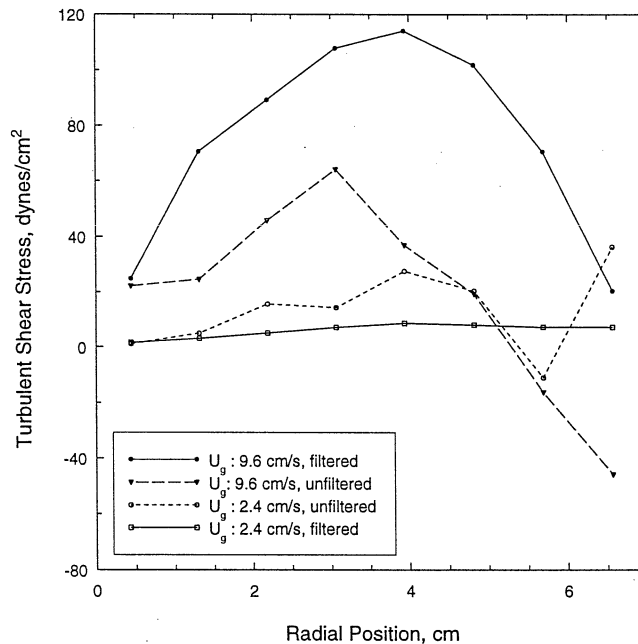

Figure 3.26: Comparison of the Turbulent Shear Stresses Before and After Filtering in a 14 cm Column

Filtering of CARPT data using the wavelet-based algorithm thus helps in reducing the level of noise in the data by 80 to 90 %, and therefore enables a better and more accurate estimation of the fluid dynamic parameters in bubble columns. Results from CARPT experiments, subject to filtering, have been successfully compared

with experimental data in the literature, and hence provide a means of validating the CARPT measurements in bubble columns. Details of these comparisons are given in Chapter 4, along with a discussion of all the experimental results.